Università degli Studi di Padova
Dipartimento di Fisica ed Astronomia
Corso di Laurea Magistrale in
Fisica

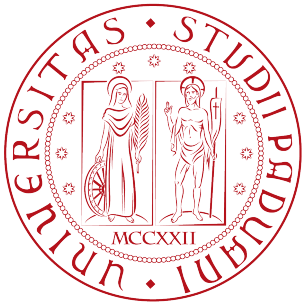

Tesi di Laurea Magistrale

Tomographic imaging with fast neutrons

Relatori:
dott. Jose Javier Valiente-Dobón
dott. Jon Wilson
dott. Grzegorz Jaworski
dott. Daniele Mengoni

Laureando:
Alberto Da Re
Matr. 1108489

Anno Accademico 2016/2017

Contents

1 Introduction

The first X-ray image was taken by Wilhelm Conrad Röntgen on December 22, 1895, and then Allan M. Cormack and Godfrey N. Hounsfield won the Nobel Prize in Medicine in 1979 for the first X-ray computed tomographic images.

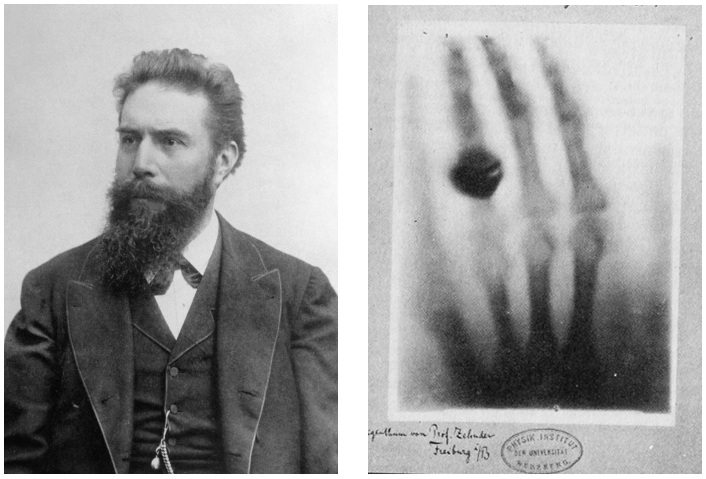

Figure 1.1: Wilhelm Röntgen and the first medical X-ray image of his wife Anna Bertha Ludwig's hand.

The aim of this work is to investigate the feasibility of performing a tomographic imaging with a highly collimated fast neutron beam. In particular, the neutron beam was produced by the unique directional neutron source LICORNE at ALTO facility of IPN Orsay [1], using the inverse kinematic reaction p(^{7}Li,n)^{7}Be, and for the neutron detection the new generation neutron detector array NEDA was used [2].

Similarly to other tomographic techniques, the idea is to measure the absorption of the beam after it has passed through the object that is under analysis. In the classical X-ray imaging, a narrow pencil beam is passed from the x-ray source to the x-ray detector [3]. The source and the detector are then translated to obtain a complete view, and a 360° scan is obtained by rotating the system (about o.3° to 1° increments) and repeating the translation process. When using neutron sources, it is not possible to move the source and the detector, so instead a specifically designed turntable was built to move the scanned sample, both perpendicularly to the beam axis and around its own vertical axis. The difference is that in this case the rotation occurs simultaneously to the translation. The final image is than reconstructed by taking each view containing the absorption information and *smearing* it along the path it was originally acquired. The result is a two-dimensional image of the scanned object: the word tomography means "a picture of a plane".

The interest in using a neutron beam is due to the complementarity of such technique with respect to the commonly used X-rays. In fact, while X-rays are strongly absorbed by high-Z materials, but pass easily through low-Z ones, fast neutrons penetrate high

Z-materials and instead are easily scattered by low-Z ones. Figure 1.2 shows the mass attenuation coefficient for various elements and different types of radiations. Clearly, there is a vast difference between X-rays (black line) and fast neutrons (red squares).

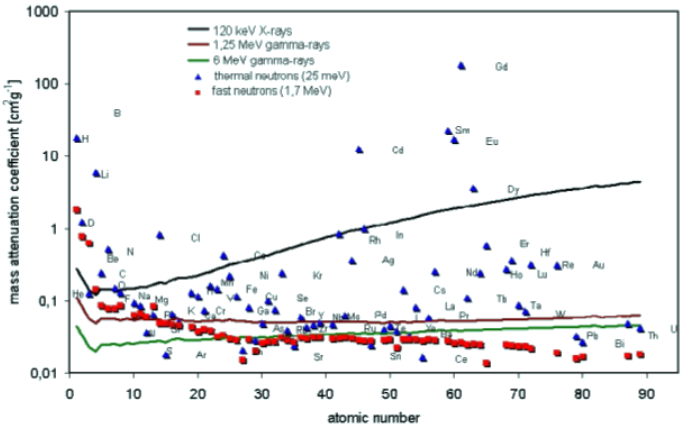

Figure 1.2: Mass attenuation coefficients for X-rays, gamma-rays, thermal neutrons and fast neutrons as a function of the atomic number of the nucleus.

The advantages of using fast neutrons instead of thermal neutrons are that the latter could possibly be captured by some elements in the scanned object, causing its activation, and that their mass attenuation coefficient has a complicated behavior changing from material to material (see Figure 1.2), and so the elements analysis would not be uniform. Furthermore, accelerator-based fast neutron sources could potentially be miniaturized and thus built anywhere, while thermal neutron sources require a reactor, preventing some applications, such as for example border security.

Fast reactor-based sources are difficult to use because fast and thermal neutrons coexist in the neutron spectrum. On the other hand, very little research work has been done for tomography with accelerator-based fast neutron sources, due to the difficulty to produce finely collimated neutron beams and high fluxes simultaneously. The unique LICORNE directional neutron source combines naturally collimated neutron beams with high neutron fluxes, and in particular very narrow neutron cones can be achieved (less than 5° opening angle) near the reaction threshold. The potential applications of fast neutron tomography are vast, covering fields as diverse as archeology, medicine, nuclear safeguards, airport security, nuclear waste characterization, etc.

The experiment was performed in December 2016: after the preparation of the setup, several scans were performed, changing the energy of the primary ^{7}Li beam as well as the analyzed object.

Initially, several short runs were taken without any object (about 10 minutes per run), starting from a ^{7}Li energy of 14.80 MeV, near the threshold of the reaction, up to 16.70 MeV, for a total of thirteen ^{7}Li different energies. These runs were then used to study the characteristics of the neutron beam itself, e.g. the correlation between the lithium energy and the beam angular opening. In fact, this was the first time that the

LICORNE neutron beam was actually detected and analyzed in its whole width, thanks to the nineteen neutron detectors array NEDA.

After that, different objects were put between the neutron source and NEDA, on the designed turntable, and 360° scans were performed of a duration of 6 hours. The first object analyzed was a compote, due to the simplicity of its shape (basically a cylinder), and its chemical composition of very light elements, that guarantee a strong neutron attenuation. Then, two cylindrical metallic boxes with unknown content, both sealed with welded bolts, were scanned separately. The purpose indeed was to blindly try to identify the objects inside. Finally, two heavy metals of known shapes were used too, with a scan only 2 hours long.

Probing a material with neutrons provides the opportunity for the development of a totally new technique: with the neutron beam in fact it is possible to "enlighten" the atoms of the material via the inelastic scattering, making them shine in the gamma spectrum. Thus, through the gamma-rays detection from (n,n'γ) reactions inside the object, it is in theory possible to identify and localize the elements present in the sample. If this proves to work, this completely new technique could provide the first opportunity to perform a ≪colour≫ tomography.

The objectives of this work thus were:

- To perform a first real characterization of the neutron beam produced, as a function of the bombarding ^{7}Li energy.
- To demonstrate the capability of LICORNE, coupled with the neutron detector array NEDA, to perform fast neutron tomographic images of different complex objects.
- To perform for the first time an entirely new type of tomographic imaging, which exploits the gamma-rays from the (n,n'γ) reaction to create an image of the spatial distribution of specific elements present in the sample.

2 Neutron beam production

A directional beam of neutrons can be produced if a nuclear reaction emitting neutrons is initiated in inverse kinematics, with a heavy ion projectile bombarding a light target.

Conventional quasi-monoenergetic neutron sources produce neutrons isotropically via direct reactions on light nuclei, e.g. d(d,p)n or ^{7}Li(p,n)^{7}Be [4]. The lack of directionality means that typically less than 1% of the produced neutrons can be used for irradiating samples, the vast majority contributing to the room background instead. The neutron production via the inverse kinematic combines the best features of white neutron sources, i.e. collimated beams, and conventional quasi-mono-energetic neutron sources, i.e. high neutron fluxes at short distances. However, the literature concerning this method of

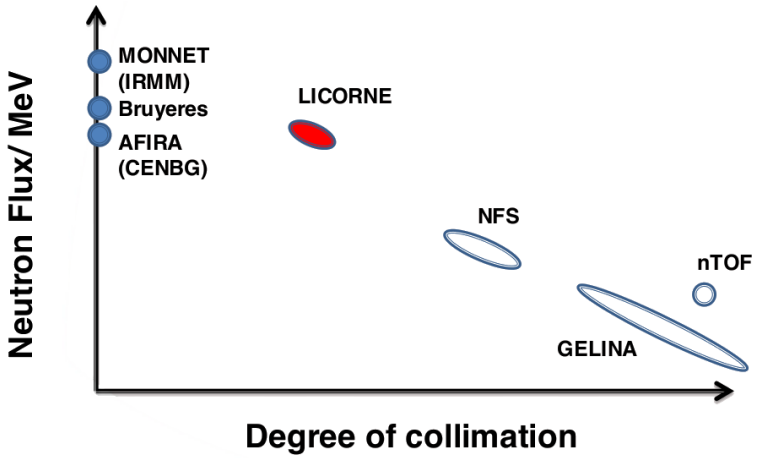

Figure 2.1: Comparison between LICORNE and other existing neutron sources, in terms of collimation and neutron flux. As can be seen, LICORNE fills a niche, presenting both a good degree of collimation and a high neutron flux.

neutron production is rather sparse: apart from a couple of test experiments performed in the early 1980s [5, 6], little detailed research has been carried out until now. At present day, the only dedicated neutron source to produce neutrons via this method is LICORNE at ALTO facility of IPN Orsay.

The focused beam clearly offers some distinct advantages, and with special attention to tomographic imaging:

1. The focusing enhances the available neutron flux by a factor between 25 and 100 [4], thus it reduces the time acquisition.

2. The lack of neutron emission at most angles results in much lower scattered neutron background.

3. The placement of sensitive detectors (i.e. gamma detectors) adjacent to the neutron source becomes feasible, without the necessity for heavy shielding.

4. As it will be clear later, especially for the gamma tomographic image reconstruction, the more collimated the neutron beam is the more spatial resolution the final image has.

2.1 The p(^{7}Li,n)^{7}Be reaction

The p(^{7}Li,n)^{7}Be reaction [7] is one of the most commonly used in direct kinematics to produce monoenergetic neutrons. If run in inverse kinematics, a strong collimation of the resulting neutron in the laboratory frame is obtained. At the reaction threshold of 13.098 MeV a monoenergetic neutron of 1.44 MeV is produced (table 2.1). With increasing beam energy new outgoing channels open, such as the production of the recoil nucleus ^{7}Be in its first excited state at 0.429 MeV. Although, in this experiment the highest energy of the incoming ^{7}Li was 16.7 MeV, namely 15.2 MeV after being attenuated through the tantalum foil that separates the hydrogen gas target from the vacuum of the beam line. Thus, only the first exit channel was populated, and the kinematics of the outgoing neutrons can easily be predicted via two-body relativistic kinematics calculations [4].

Table 2.1: Main characteristics of the p(^{7}Li,n)^{7}Be reaction. Neutrons produced in each channel are labeled as n_i to indicate they are produced with different kinematics. Taken from [4].

Type of exit channel	**Q-value (MeV)**	**Threshold energy (MeV)**	**Primary 0° neutron energy (MeV)**
n_0 + $^7_4$Be	-1.644	13.098	1.44
n_1 + $^7_4$Be* (0.429 MeV)	-2.073	16.513	3.84
n_2 + $^3_2$He + $^4_2$He	-3.230	25.726	8.18
n_3 + $^7_4$Be* (4.57 MeV)	-6.214	49.489	18.79

The kinematic curves for a given bombarding energy have two distinct peaks in the laboratory frame, corresponding to forward and backward emission of neutrons in the center of mass frame (Figure 2.2). The picture is although further complicated by the energy loss and straggling of ^{7}Li through the tantalum foil and the hydrogen target.

The gain from the focusing and natural collimation can be expressed in terms of neutron flux enhancement over the non-inverse reaction (Figure 2.3). At the threshold the emitted neutrons move with the centre of mass of the system, i.e. follow the ^{7}Li beam direction. As a consequence, close to the threshold energy, it is possible to produce very narrow ($< 5°$) cones of neutrons [6]. With increasing ^{7}Li bombarding energy, the cone broadens and the number of neutrons in a given solid angle decreases, so does the enhancement factor.

Although, the huge gain in intensity due to the kinematic focusing is offset by corresponding losses from two other factors. Firstly, the available beam current of ^{7}Li is

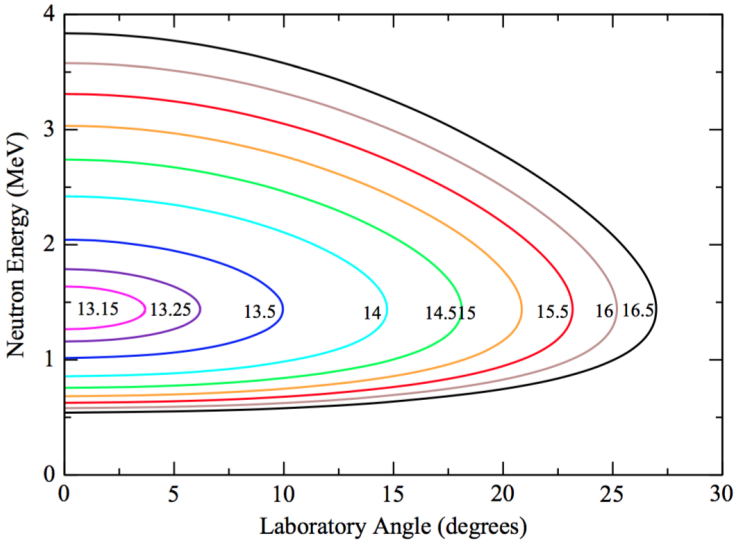

Figure 2.2: Kinematic curves relating the angle of neutron emission to neutron energy in the laboratory frame for different ^{7}Li bombarding energies from 13.15 to 16.5 MeV, calculated using two-body relativistic kinematics. Figure taken from [4].

much lower than that available for protons in the non-inverse reaction, because of the relative difficulty to extract ^{7}Li ions from the ion source. Secondly, the energy loss of ^{7}Li across a given target is higher than that for protons due to its higher atomic number.

The maximum available fluxes of up to 10^{7} neutrons/s/sr (assuming continuous ^{7}Li beam currents of 100 nA) are comparable to those available with other conventional quasi-monoenergetic neutron sources. However, the natural collimation and neutron beam directionality provides the distinctive advantages mentioned before.

The principle of LICORNE, using inverse kinematics, is not just restricted to beams of ^{7}Li [8]. Indeed, any reaction on a hydrogen target with a heavy ion beam which has a favorable Q-value for production of neutrons will work. The next most obvious reaction is p(^{11}B,n)^{11}C. Since the first excited state of ^{11}C is much higher than that of ^{7}Be (2.00 MeV compared to 0.43 MeV respectively), higher energies per nucleon, and a greater velocity of the centre of mass frame, can be achieved without ejecting the ^{11}C recoil in its first excited state. This implies that with LICORNE neutrons with final energy up to 12 MeV could be produced.

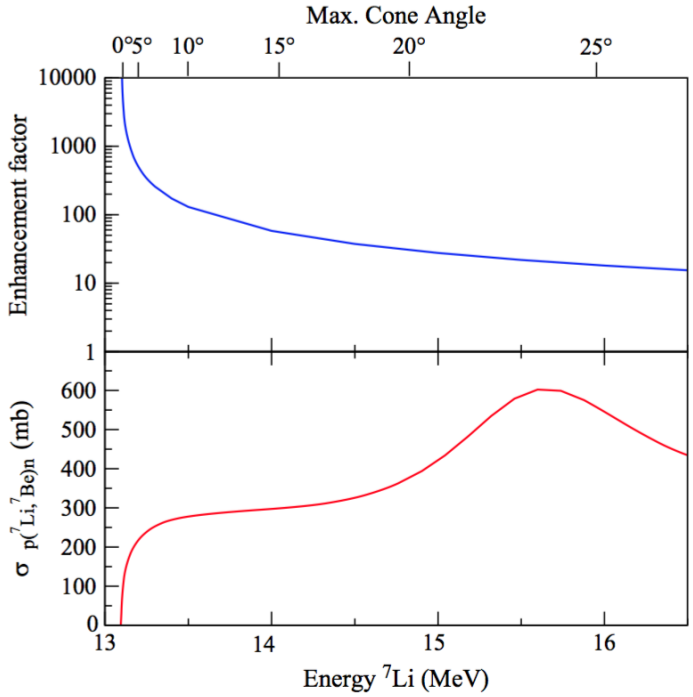

Figure 2.3: The top panel shows the enhancement factor of the neutron flux between the inverse kinematic and the direct kinematic reaction as a function of ^{7}Li bombarding energy. The bottom panel shows the p(^{7}Li,n)^{7}Be reaction cross-section over the same energy range. Figure taken from [4].

3 Neutron detection principle

The only way neutrons can interact with matter is through the nuclear force, characterized by a short range, being then effective only in the proximity of a nucleus. In each collision the neutron transfers some of its energy to the nucleus, finally being absorbed in the material whenever its velocity is sufficiently low. In a scintillator the scattered nuclei, due to electromagnetic interaction, excite the surrounding molecules that in turn reemit the absorbed energy via photons. These photons can then be revealed by a photomultiplier (PM), that converts the light in current, via the photoelectric effect, and produces the signal.

In the neutron elastic scattering, the maximum energy transfer to the nucleus occurs for an head-on collision, i.e. for $\theta = 0$, resulting in a maximum recoil energy of [9]

$$E_{R,max} = \frac{4A}{(1+A)^2} E_n \tag{3.1}$$

where A is the mass number of the target nucleus and E_n is the energy of the neutron (from 100 keV to 10 MeV for fast neutrons). Therefore, if the target nucleus is hydrogen ($A = 1$), the entire neutron energy can be transferred in a single scattering event, while a smaller maximum energy transfer results for heavier nuclei. For example, with ^{12}C ($A = 12$) $E_{R,max} \sim 28\% E_n$ for a single scattering event.

The molecules of the scintillator, after being excited by an ionizing radiation (such as a scattered nucleus or a gamma-ray), produce the fluorescence light by the radiative decay of their excited states. Referring to Figure 3.1, the excited state can actually be a singlet (spin = 0) or, after the intersystem crossing process, a triplet (spin = 1) [9]. The transition from the singlet excited state to singlet ground state has a life time typically of the order of the nanosecond, while the transition from the triplet excited state to the singlet ground state is of the order of the millisecond (due to the forbidden transitions from triplet states to singlet states). Molecules in triplet states can however interact pairwise resulting in one molecule in the ground state and one molecule in an excited singlet state, which then will decay. This interaction is much faster than the decay of the triplet states, but still slower than the decay of the singlet states, and therefore the triplet states recombination will give rise to a slow component in the light collection from the scintillator material. If the particle that is stopped has a high specific energy loss, the density of the excited molecules will be very high, and there will be a greater interaction between the triplets, causing a larger slow component in the output from the scintillator. This will be the principle behind neutron-gamma discrimination.

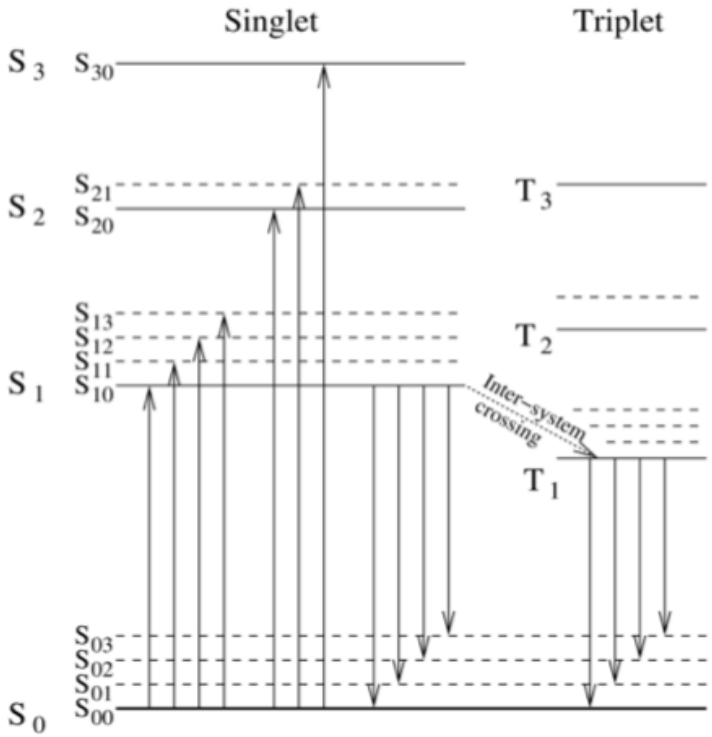

Figure 3.1: Energy states of molecules with π-electron structure. Figure taken from [9].

4 Tomographic image reconstruction

As for all tomographic imaging, the idea is to probe the object along different directions in a plane, and use the absorption information to create a two-dimensional image of the object itself. Usually, in common X-rays computed tomography (CT), the source of the radiation and the detectors are moving around the object being scanned [3]. Thus, in the end, many different absorption spectra are obtained, each one from a different view (see Figure 4.1). Although, since it is not possible to move the neutron beam source,

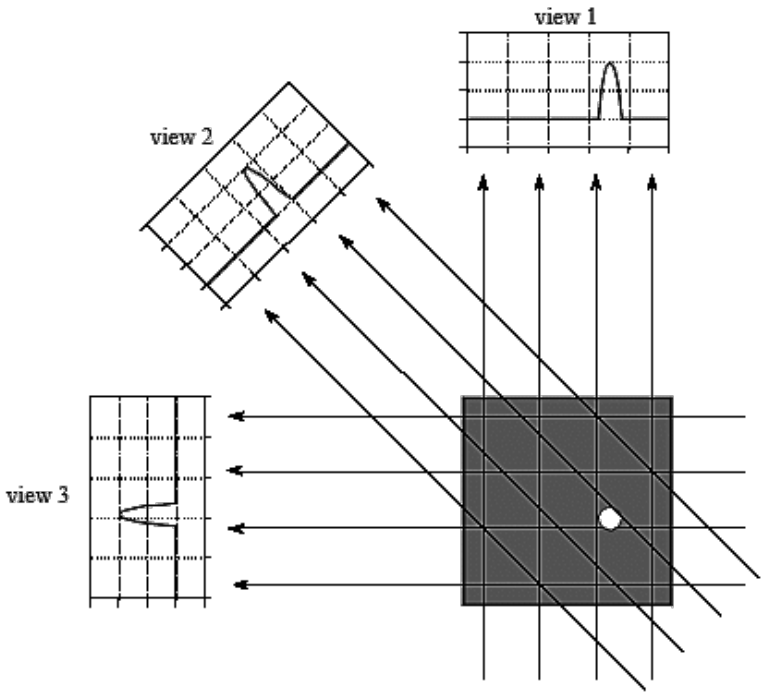

Figure 4.1: CT views. Each point of the spectra represents the absorption along the corresponding trajectory. While only three views are shown here, a typical CT scan uses hundreds of views at slightly different angles. Figure taken from [3].

the object is moved instead. A special turntable was built, with a circular section of 30 cm diameter, which could perform a translation perpendicularly to the beam axis and simultaneously a rotation around its own axis. In this way, at the end of the scan, the object is probed along all directions in the horizontal plane.

Two coordinate systems can be defined: one (x, y) integral with the turntable, with its origin in the center, and one (x', y') integral with the laboratory frame, positioned in the intersection between the neutron beam axis and the path of the turntable (see Figure 4.2).

For every table position x' and orientation ϕ a certain neutrons count was measured by NEDA, and going through a full 360° cycle a *sinogram* is obtained. In CT reconstruc-

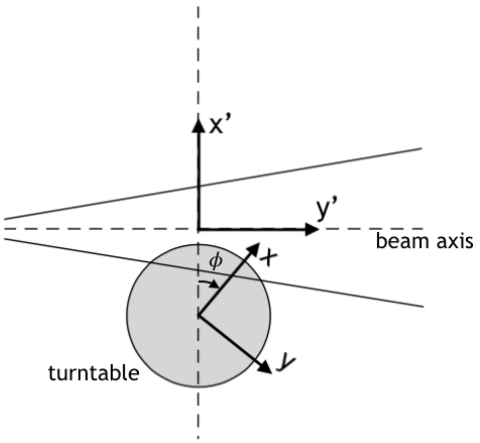

Figure 4.2: Defined coordinate systems.

tion a sinogram is simply the two-dimensional array of data containing the absorption (transmission) information at (x', ϕ) [10] (see Figure 4.3).

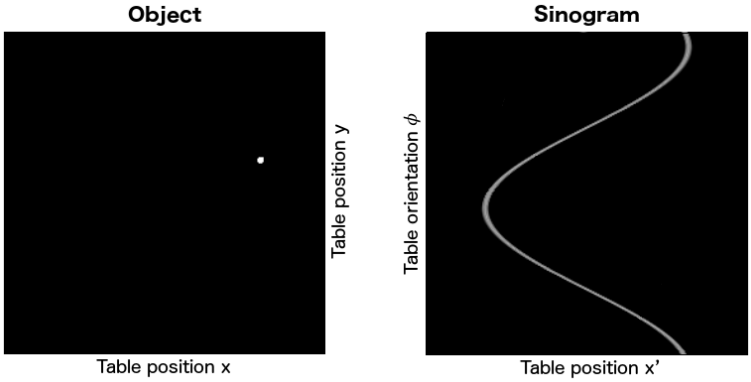

Figure 4.3: An example of a sinogram. On the left a point object is shown; on the right, the corresponding sinogram shows the absorption value at each table position and orientation (a black point indicates that all the beam has passed through, a brighter point indicates that some of the beam has been absorbed). It is clear why the name "sinogram".

To pass from the sinogram to the two-dimensional image an algorithm was developed during the analysis, based on the original code written by Basia Wasilewska. This algorithm is based on the *back-projection* technique: the final image is reconstructed by taking each view and smearing it along the path it was originally acquired [3] (see Figure 4.4). Whenever a neutron is detected by NEDA, the position of the beam cone with respect to the table is correctly reconstructed, and then the corresponding area

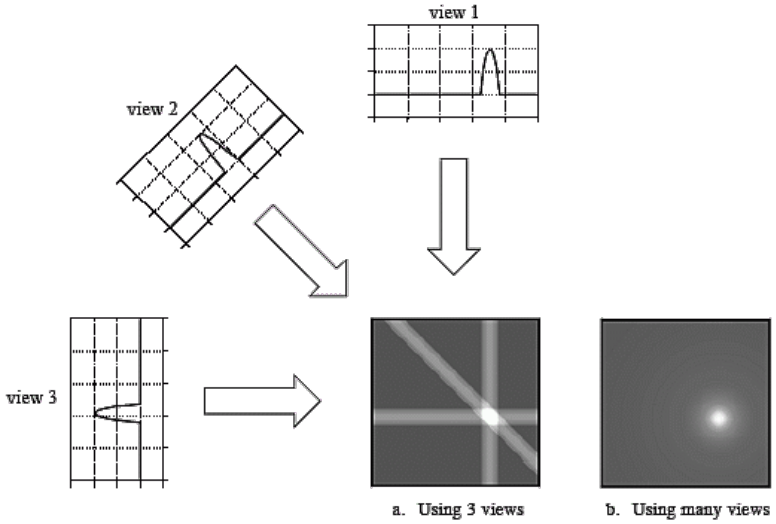

Figure 4.4: Back-projection from the measured spectra to the real image. For each view, the absorption (transmission) information is smeared along the corresponding beam path. After many views, the real two-dimensional image of the object is created. Figure taken from [3].

inside the table is filled with one event, as shown in Figure 4.5. For every (x', ϕ) event, the algorithm moves along all the y' covering the table area (from y' = -15 cm to y' = $+15$ cm), and for each one it runs through all the other x' inside the beam cone (from x' $- tg(\alpha) \cdot$ (y' + D) to x' $+ tg(\alpha) \cdot$ (y' + D), where α is the cone half-width and D = 21.75 cm is the distance between the source and y' = 0). In every step, if the point is actually inside the table, i.e. if $x'^2 + y'^2 < 15^2$, the proper (x, y) point of the table is filled, where:

$$\begin{aligned} x &= x' \cdot cos(\phi) + y' \cdot sin(\phi) \\ y &= x' \cdot sin(\phi) - y' \cdot cos(\phi) \end{aligned} \tag{4.1}$$

after a y $\rightarrow -$y reflection just for a graphic purpose. In this way, the image is reconstructed with respect to the table itself.

For the neutron reconstruction the cone can be restricted to the opening angle of each NEDA detector, since it is possible to identify the specific detector that registered the event. For the gamma analysis instead, all the beam width has to be used, because the inelastic scattering between the neutron and a nucleus of the sample which produces the photon may have occurred everywhere along the probed region. The algorithm has been adapted for the gamma analysis, and it will be explained in Section 9.

Finally, different possible corrections were studied and, if showed to improve the final reconstruction without introducing bias or distortions, implemented in the final algorithm.

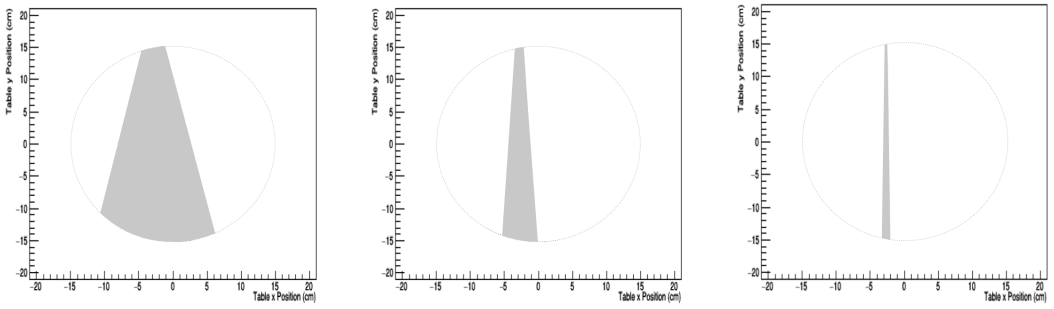

(a) (b) (c)

Figure 4.5: Reconstruction of one event. The gray cone corresponds to the position of the beam with respect to the table, while the dotted line marks the edge of the table itself. In (a) all the nineteen NEDA detectors are used, in (b) just the ones inside the beam width, while (c) corresponds to only the angular opening of the central detector.

5 Experiment

In this section, the experimental setup will be discussed.

5.1 LICORNE

The LICORNE neutron source sits in an aluminium chamber of approximately 17 cm diameter [11].

Figure 5.1: The LICORNE neutron source.

The first version of LICORNE used rotating polypropylene disks as the hydrogen target [8]. This had the advantage of fine control over the thickness of the target and hence the number of hydrogen atoms in the path of the ^{7}Li beam. Thickness could be varied between 4 μm and 100 μm. However, the major drawback was the production of unwanted parasitic neutrons from fusion evaporation reactions of ^{7}Li with the ^{12}C in the polypropylene polymer. The presence of secondary unwanted neutrons is a particular problem for the Ge detectors, since their sensitivity to neutron damage. In addition, the radiation damage of the polypropylene at the highest intensities caused the rapid loss of hydrogen from the polypropylene, and targets needed to be changed every few hours, with the need to break the vacuum ($< 10^{-5}$ atmospheres).

To solve these problems, a new hydrogen gas target had been developed. The goal was to suppress all secondary reactions via the use of high Z materials in the construction of the collimator, the thin entrance window and the beam stop, which are made of tungsten, tantalum and lead respectively.

To achieve fine control over the number of hydrogen atoms in the path of the beam, four aluminium cells (0.5 mm thick) have been made of lengths 2, 3.5, 5.5 and 7.5 cm

respectively. The pressure of the hydrogen gas in the cell can be varied between 1 and

Figure 5.2: The exchangeable gas cells of different lengths (7.5 cm, 3.5 cm and 2 cm).

2 atmospheres, giving and additional flexibility to control the shape of the resulting neutron spectrum. The number of hydrogen atoms per cm^2 in the target can thus be varied very precisely over almost an order of magnitude between 1.0×10^{20} and 8.0×10^{20}. The tantalum entrance window is 5 mm in diameter and between 2 μm and 4 μm thick and is designed to resist in the most extreme range of pressure and beam current (2 atm and 100 nA).

Optical and infrared cameras are included for beam tuning and inspecting the targets from inside without having to break the vacuum. The beam spot is tuned by placing a retractable phosphorescent target in the path of the beam.

To prevent air (and oxygen) entering the gas cell, a flow of hydrogen through the gas control system is maintained via a flow meter and a needle valve. The flow is very low and typically of 30 cm^3 per minute. The hydrogen is evacuated outside the accelerator buildings to prevent potentially explosive build-ups of gas. In the event of a rupture of the cell window, two safety valves will close rapidly when sensors detect any minor changes in pressure, and the flow of hydrogen from the gas bottle is cut off.

The neutron fluxes with the hydrogen gas cell are higher than those available with the rotating polypropylene disc system. The reason is that the stopping power per unit loss of ^{7}Li energy for hydrogen is less than that for polypropylene, so more hydrogen atoms can be placed in the path of the beam for a given energy loss. Figure 5.4 shows calculations for achievable fluxes at varying distances from the front face of the cell as a function of the incident ^{7}Li energy. As the energy becomes nearer the threshold, the neutron cone opening becomes smaller and the diminution of the flux becomes less severe as a function of distance [8].

The gas cell used for the experiment was 2 cm in length with a pressure of 1.2 atm and a tantalum window of 2.7 μm thickness.

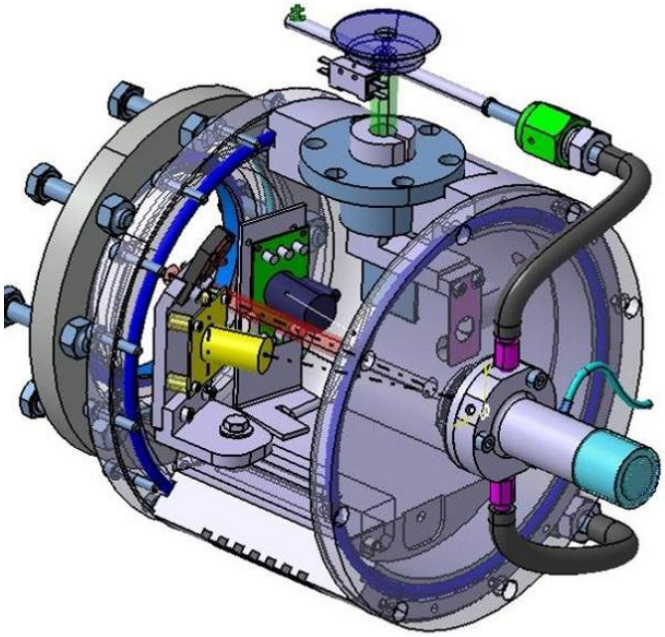

Figure 5.3: The design of LICORNE, including optical and infrared cameras for monitoring the focussing of the beam on the thin tantalum window separating the vacuum from the gas cell. Figure taken from [8].

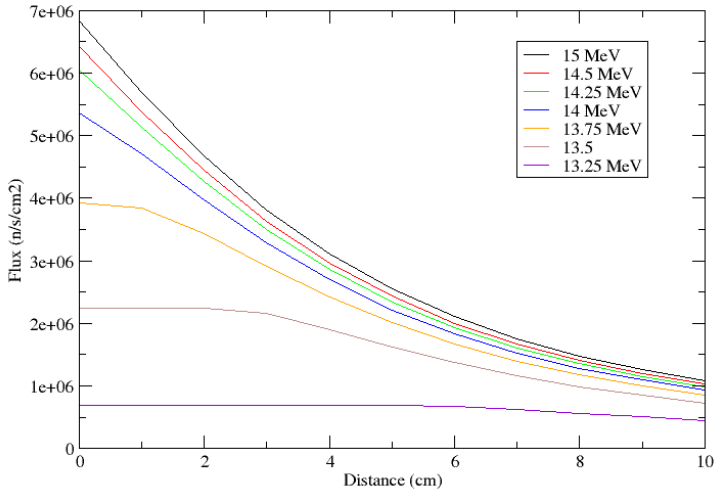

Figure 5.4: Available neutron fluxes at zero degrees as a function of the distance from the gas cell for different ^{7}Li beam energies. Figure taken from [8].

5.2 NEDA

The NEutron Detector Array, NEDA [12, 13], is the future state-of-the-art neutron multiplicity filter which will operate as the ancillary device for the most advanced gamma-ray spectrometers in Europe, such as AGATA [14], EXOGAM [15] or GALILEO [16]. The design goal was to build an array with the highest possible neutron detection efficiency, excellent neutron-gamma discrimination (NGD), and a very small neutron scattering probability. This work represented the first in-beam experiment which involved this new-generation neutron detector.

Each module consists of an hexagonal cylinder of aluminium with a thickness of 2 mm, a length of 200 mm and a diameter of 127 mm (see Figure 5.5), containing about 3 liters of EJ301 liquid scintillator [17]. The optimization of the length had been

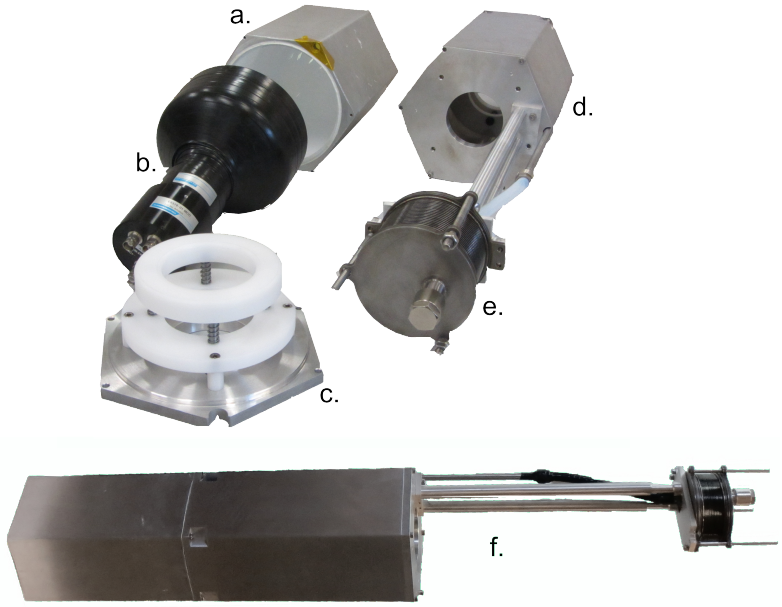

Figure 5.5: One NEDA detector. Above, the single parts are shown: (a) hexagonal cell containing the EJ301 scintillator; (b) R11833-100 PM; (c) holding cover for the PM; (d) hexagonal case for the PM; (e) expansion bellows for the liquid scintillator. μ-metal is within the hexagonal case of the PM, to shield from the external electromagnetic field, including the Earth one. Below, the mounted prototype can be seen (f).

studied [12], and the result is that for a 200 mm detector length the detection probability is of the order of 70%, minimizing the probability of cross-talk. A bellows, connected to the detector through a stainless steel tube, keeps the scintillator at a constant pressure, expanding or contracting in according to the temperature. For the conversion from scintillation light to a voltage signal a R11833-100 superbialkali PM from Hamamatsu, with a quantum efficiency of 43% [18], is mounted on each detector using an optical grease. Digital algorithms describing the performance of the NEDA detectors in details,

by quantifying their timing and neutron-gamma discrimination capabilities, are being developed at LNL-INFN, in Italy [19, 20].

5.3 Setup

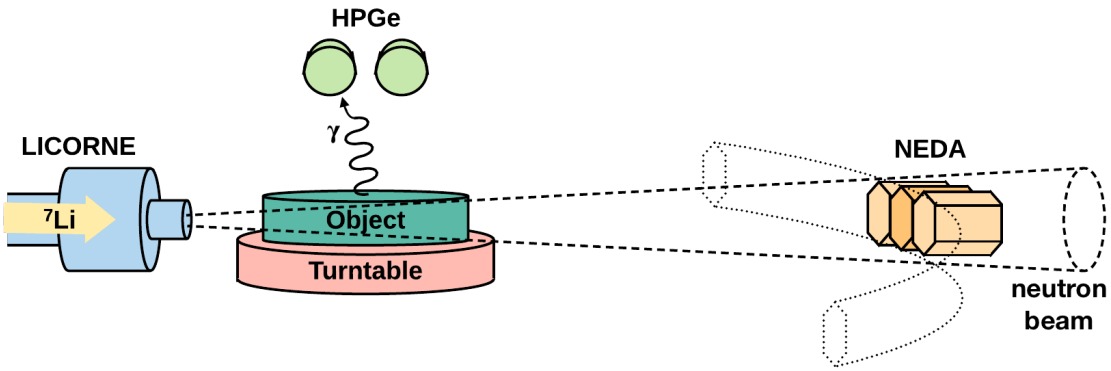

Figure 5.6: Experimental setup.

The experimental setup saw the LICORNE neutron source operating with a pulsed ^{7}Li beam (400 ns between each pulse) on a 2 cm thickness hydrogen gas target. The energy range of the incoming ^{7}Li went from a minimum of 14.80 MeV to a maximum of 16.70 MeV. The specifically designed turntable was placed at 6.75 cm from the LICORNE exit window, with its center at 21.75 cm having a diameter of 15 cm (see Figure 5.7). It

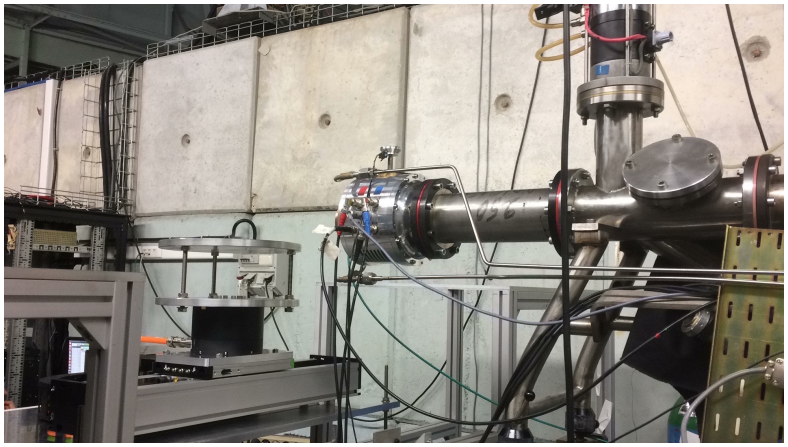

Figure 5.7: LICORNE (on the right) and the turntable (on the left).

was designed to be rotated precisely in angle (1 degree steps) and shifted in the direction perpendicular to the beam axis by up to 15 cm in both directions ($\sim$ 3 mm steps). On

top of it were placed a compote, two different cylindrical metallic boxes with unknown contents, and two heavy metals with paraffin (see Figure 5.8) in order to be scanned.

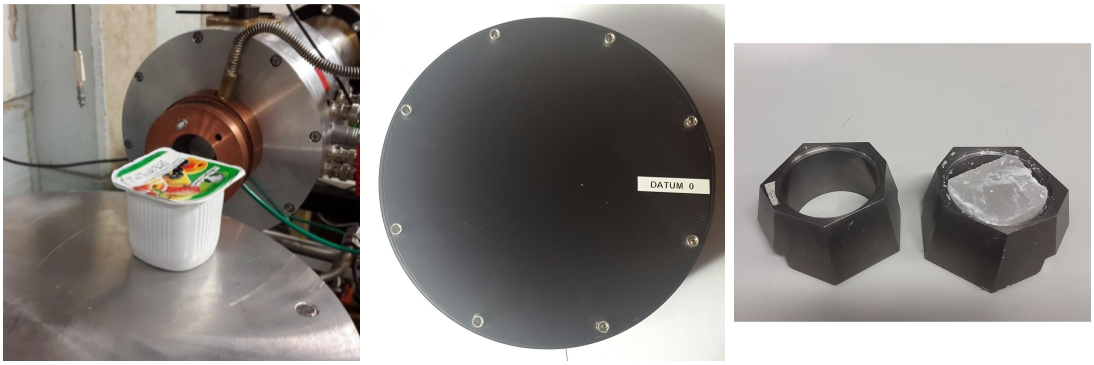

(a) (b) (c)

Figure 5.8: (a) Compote positioned on the turntable in front of LICORNE exit window, (b) one of the two metallic boxes with unknown contents, and (c) the two heavy metals with paraffin.

The NEDA array for the measurement of the neutron beam consisted of an arc of nineteen detectors at a distance of 480 cm from the LICORNE exit window. Each neutron detector thus defined a cone of about 1.5° opening angle, and the total arc was 30° wide.

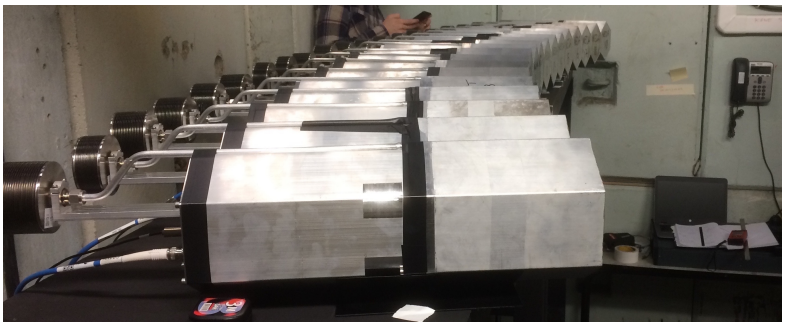

Figure 5.9: Side view of the nineteen NEDA detectors arc.

Two Ge detectors were placed 13 cm above the turntable, and cooled with liquid nitrogen for more than 24 hours before the data acquisition with the beam. Each one had a Pt100 resistance thermometer to check the temperature. However, one of the two did not prove to work, so eventually in the analysis only one was used.

The read-out of the detectors was carried out with Faster 12-bits 500 Msps digitizers [21], which allowed to define four integration gates in the FPGAs. This enabled having NGD parameter online. In addition, time-of-flight (TOF) was measured as a difference between RF and time-to-digital converters (TDC) implemented in the Faster

digitizers. The gamma-flash was used during the analysis to align all the NEDA detectors to the same time reference.

5.4 Detectors calibration

The energy calibration was performed both for NEDA and the Ge detectors.

For NEDA, four different reference gamma-sources were placed right in front of each cell, precisely ^{22}Na, ^{60}Co, ^{137}Cs, ^{241}Am. For each one, the position of the Compton edge (CE) was measured, with the exception of ^{241}Am, for which the photopeak could be used instead. Simulations [12] prove that the peak of CE is placed at 90% of it's real energy, thus the corresponding values is to be used, as shown in Table 5.1. With a linear interpolation, the channel-to-energy conversion for each NEDA detector was obtained.

Table 5.1: The four sources used for the calibration of NEDA.

Source	**γ energy (keV)**	**CE (keV)**	**90% CE (keV)**
^{22}Na	511.0, 1274.5	340.7, 1061.7	306.6, 955.5
^{60}Co	1173.2, 1332.5	963.4, 1118.1	867.1, 1006.3
^{137}Cs	661.7	477.3	429.6
^{241}Am	59.5	-	-

For the Ge detectors instead, three characteristic gamma peaks were used to calibrate the energy spectrum: the 511.0 keV annihilation peak, the 1460.8 keV from ^{40}Ar (present in the room), and the 2614.5 keV from ^{208}Pb (constituting the lead shieldings and the beam stopper). Also in this case, through a linear interpolation the calibration parameters were obtained.

6 Neutron-gamma discrimination

For a correct neutron detection it is crucial to discriminate the actual neutrons from the signals produced by gammas [22]. As discussed in Section 3, the NGD is based on the difference between the slow components of the signal produced. The scattered nucleus, after the interaction with the neutron, has a higher specific energy loss compared to the electron ionized by the gamma. Thus, the density of the excited scintillator molecules will also be higher, and so will be the probability of triplets recombination. Hence, the slow component from the detection of a neutron will be greater than the one from the detection of a gamma (as pictured in Figure 6.1).

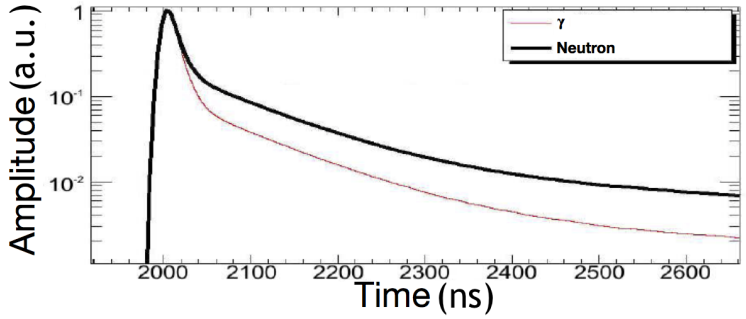

Figure 6.1: Pulse shape difference between a neutron and a gamma-ray interaction for a liquid scintillator.

In the pulse shape analysis (PSA), the integral on the slow component is compared to the total integral of the signal, and a different ratio between the two is expected depending on the particle which was detected. In other words, for a signal produced by a neutron the slow-to-total ratio will be higher than for a signal coming from the detection of a gamma, being higher the slow component. This is known as the *Charge Comparison* method [23].

6.1 PSA parameters optimisation

Before starting to scan the samples, the optimization of the NEDA NGD parameters was performed. Referring to Figure 6.2, the integration for the total signal was performed between a_1 and a_3, while the integration for the slow component between a_2 and a_3. For the optimization, the position of a_2 had been changed, looking for the best NGD. In particular, a_1 and a_3 were set to -20 and 400 ns respectively, while six different values where studied for a_2, from 20 to 45 ns. For each parameters set, the NGD capability was evaluated through the figure-of-merit (FOM):

$$\mathrm{FOM} = \frac{|\mathrm{P_n} - \mathrm{P}_\gamma|}{\mathrm{FWHM_n} + \mathrm{FWHM}_\gamma} \tag{6.1}$$

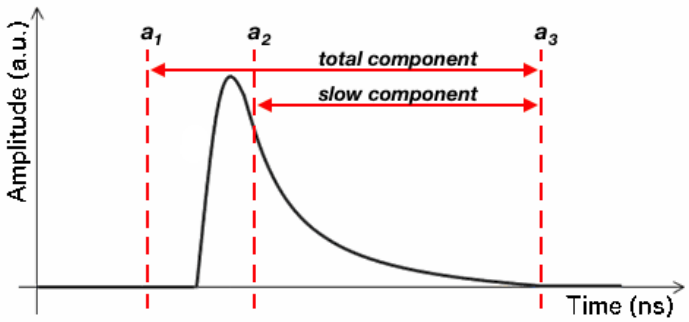

Figure 6.2: The slow and the total component of the signal, with the three parameters that define the integration range.

where $P_{n(\gamma)}$ is the position of the neutron (gamma) peak in the distribution spectrum of the discrimination parameter (i.e. the slow-to-total ratio), and $FWHM_{n(\gamma)}$ is the corresponding full width at half maximum value. A larger FOM normally indicates a better NGD performance. However, it should be noted that the FOM only measures the degree of separation that can be achieved between different types of event distributions, and does not take into account any misidentification case [24]. For example, the misidentification due to *pile-up effect* (the overlapping of one signal with the following one) is quite common when the count rate is vey hight, but the two peaks are still well separated.

Displaying the slow-to-total ratio versus the total integral of the signal (see Figure 6.3), two distinct groups of events can be seen, the upper one corresponding to neutrons and the lower one to gammas.

After an y-projection of the region between 52 and 212 keV, the distribution of the slow-to-total ratio is shown in Figure 6.4. Through a gaussian fit on each peak, the corresponding FOM is obtained. In Table 6.1 the different FOM for different set of the parameter a_2 are listed. As can be seen, the best values corresponds to a a_2 parameter

Table 6.1:

a_2 **(ns)**	**FOM**
20	1.69 ± 0.01
25	1.83 ± 0.01
30	1.86 ± 0.01
35	1.878 ± 0.009
40	1.883 ± 0.009
45	1.81 ± 0.01
60	1.659 ± 0.009

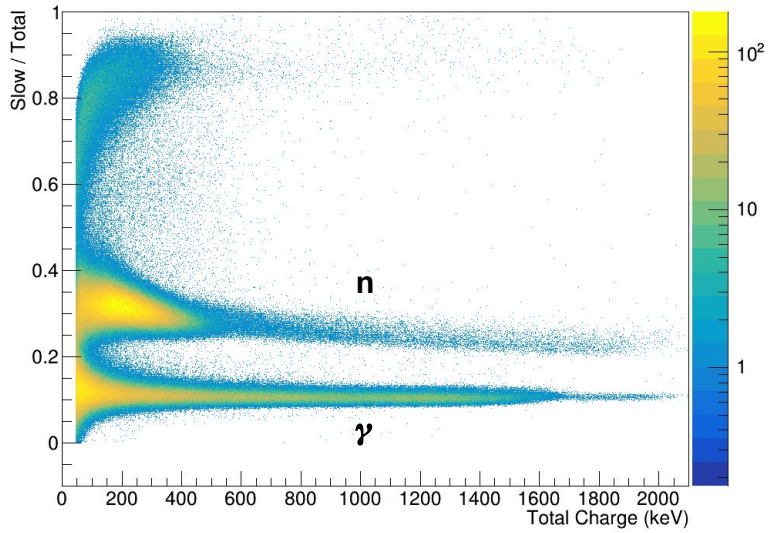

Figure 6.3: Slow-to-total ratio versus the total charge deposited in NEDA. ^{7}Li energy was at 15.25 MeV, and $a_2 = 30$ ns.

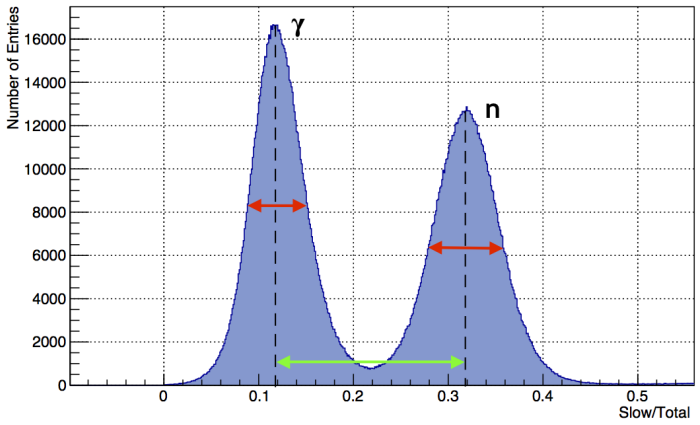

Figure 6.4: Distribution of the slow-to-total ratio, taken as the PSA parameter to distinguish between neutrons and gammas. ^{7}Li energy was at 15.25 MeV, $a_2 = 30$ ns, with a total energy cut between 52 and 212 keV. The FOM is obtained from the ratio between the distance between the two centroids (green arrow) and the sum of the two FWHM (red arrows).

between 30-40 ns. During the data acquisition with the various samples, of the four integration gates of the FPGAs, one was defined from -20 to 400 ns for the total charge deposited in NEDA, and the remaining three respectively from 30, 45, 60 to 400 ns for the integration of the slow component. Thus, the best integration gate for the slow component was taken as the one starting at 30 ns.

Together with the slow-to-total ratio, another parameter useful for the NGD is the time of flight: where neutrons will have a wide range of TOF depending on their energy distribution, gamma-rays will produce a much faster and narrower peak. In Figure 6.5 both the parameters are used to separate the neutron events from the gamma ones. During the analysis, a gate on the neutron blob can be made to select only the events coming from the detection of the neutron beam.

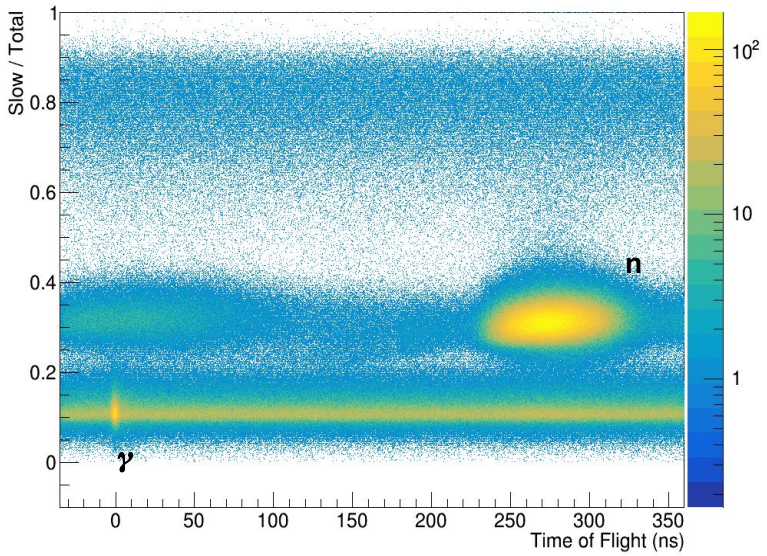

Figure 6.5: Slow-to-total ratio versus TOF. The gamma-flash and the prompt neutrons from the beam can clearly be seen. Above the gamma-flash, the backscattered neutrons from the wall form a second blob; they belong to the previous pulse, so their actual time of flight is 400 ns greater. At the same level of the gamma-flash there is a constant distribution of gammas from the room background. ^{7}Li energy was at 15.25 MeV, and $a_2 = 30$ ns.

7 Beam characterisation

The presence of the neutron detectors arc allowed to have a real-time measurement of the beam profile along all its width. Several different energies of the incoming ^{7}Li were used and the resulting neutron beam was studied. On top of Figure 7.1 it is shown the counts for each NEDA detector of the arc with a ^{7}Li energy of 15.00 MeV. The bump around the central region is clearly indicating the center of the neutron beam, but there is still a lot of background covering the real shape of the beam itself. After performing the gate on the PSA parameter and TOF, the real neutron beam profile can be obtained, as shown in the bottom of the same figure. Each detector was also normalized on the gamma-flash intensity, which is known to be isotropic and hence uniform at all angles, in order to eliminate any possible difference in the performance of the detectors.

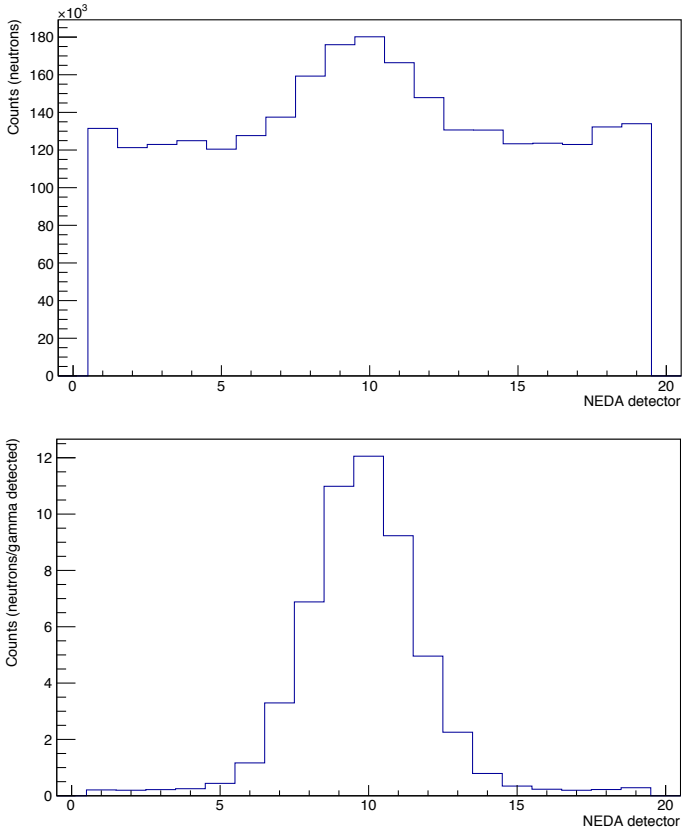

Figure 7.1: Neutron beam profile, before (top) and after (bottom) the gate on the PSA parameter and TOF and the normalization with the gamma-flash intensity. ^{7}Li bombarding energy at 15.00 MeV.

The characteristics of the produced neutron beam as a function of the ^{7}Li energy were studied, i.e. the beam width and intensity. Different runs were taken without any sample, for the duration of about 5 min each, increasing progressively the energy of the

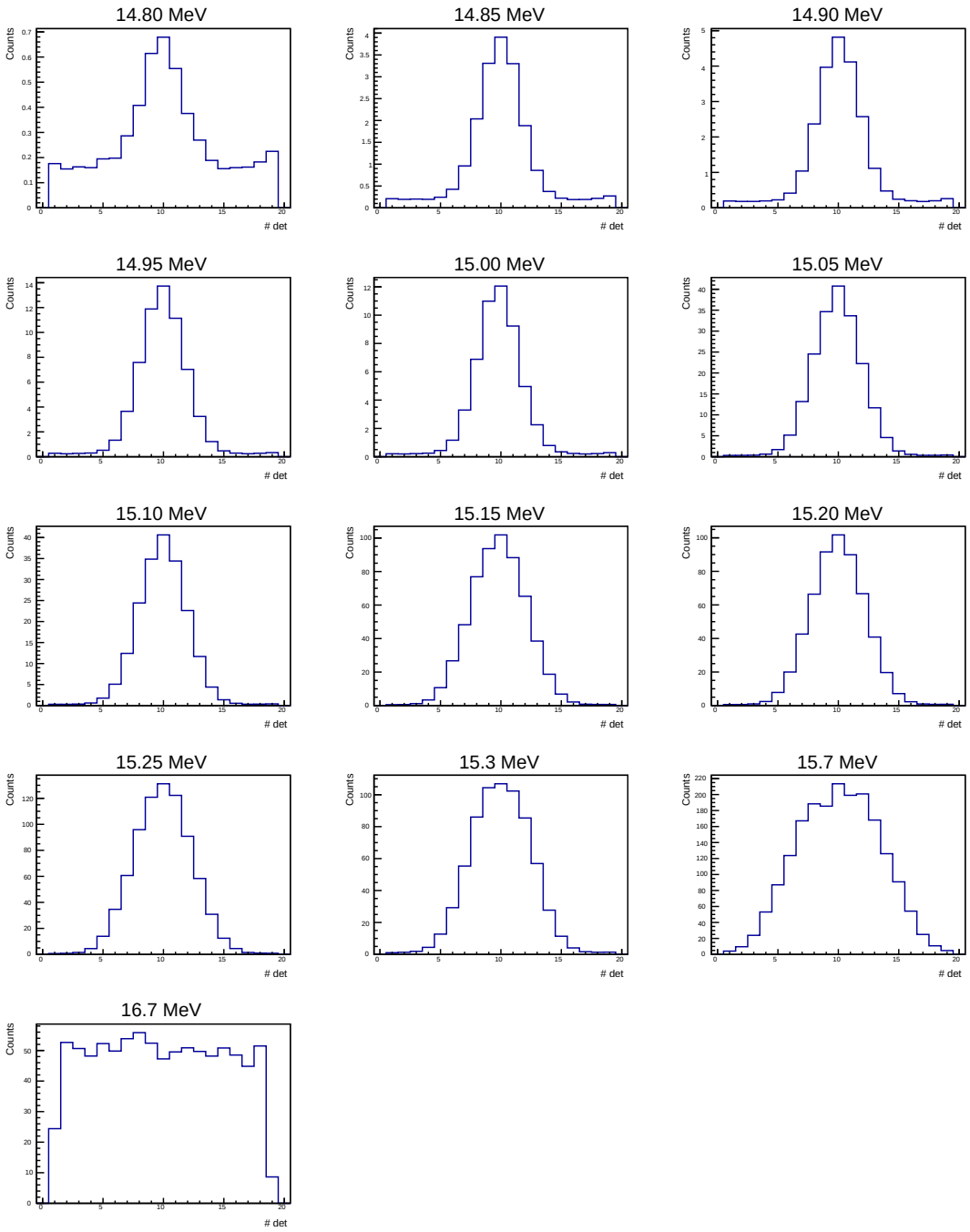

Figure 7.2: Evolution of the neutron beam profile with increasing ^{7}Li energy.

bombarding lithium from 14.80 MeV to 16.70 MeV. In Figure 7.2 the evolution of the neutron beam can be observed.

In particular, for each different run, the beam width and intensity were calculated respectively as the FWHM and the integral of the gaussian fit of the neutron beam profile (see Figure 7.3). The results are listed in Table 7.1. Note that the 16.7 MeV ^{7}Li

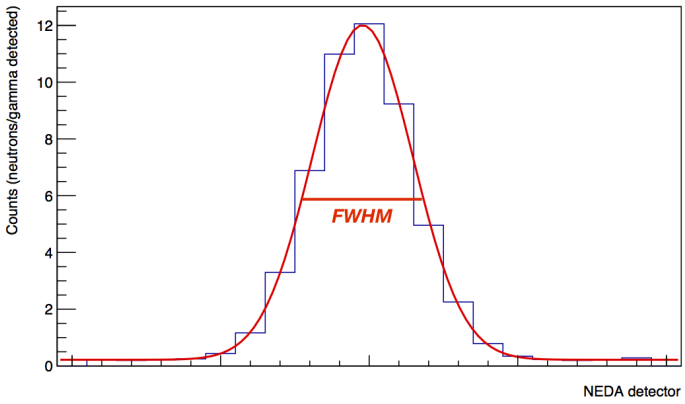

Figure 7.3: Gaussian fit of the neutron beam profile. ^{7}Li energy at 15.00 MeV.

energy case was excluded, since for this energy the beam exceeds the angular coverage of the NEDA arc (30°), so it was not possible to estimate the full beam width nor its total intensity.

In Figure 7.4 it is shown the beam half-width θ as a function of the ^{7}Li bombarding energy, and the interpolation with the best fitting function results in a quadratic dependence, i.e.:

$$\theta = 3.207(2) \cdot {E_{^7\mathrm{Li}}}^2 - 93.34(3) \cdot E_{^7\mathrm{Li}} + 682.4(3) \tag{7.1}$$

where θ is measured in deg and $E_{^7\mathrm{Li}}$ in MeV.

Looking at the relation between the beam width and its intensity, a linear dependence is found (see Figure 7.5):

$$\mathrm{I} = 530(10) \cdot \theta - 1590(50) \tag{7.2}$$

which could be very useful also for future experiments in order to find the right compromise between the two quantities depending on what is needed. The intensity I is measured as the number of neutrons per gamma detected.

The final energy of the produced neutrons, obtained from TOF, was also studied as a function of the ^{7}Li bombarding energy. As previously reported (Subsection 2.1), the two-body kinematics leads to the production of two distinct peaks, one with higher neutrons energy (corresponding to forward emission in the CM) and one with lower one (corresponding to backward emission in the CM). Looking at Figure 2.2, it can also be noted that the relative distance between the two peaks, at 0°, is increasing with the ^{7}Li energy. For this reason, and due to the deterioration of the energy resolution

Table 7.1: Neutron beam characteristics for the different ^{7}Li bombarding energy used.

^{7}Li energy (MeV)	**Beam half-width (deg)**	**Beam intensity (neutrons/γ detected)**	**Neutron energy at 0° (MeV)**
14.80	2.92 ± 0.05	5.31 ± 0.05	1.5 ± 0.1
14.85	3.00 ± 0.05	19.2 ± 0.2	1.5 ± 0.1
14.90	3.04 ± 0.05	22.9 ± 0.2	1.5 ± 0.1
14.95	3.24 ± 0.05	64.0 ± 0.6	1.5 ± 0.1
15.00	3.11 ± 0.05	54.2 ± 0.5	1.5 ± 0.1
15.05	3.54 ± 0.06	197 ± 2	1.5 ± 0.2
15.10	3.52 ± 0.06	197 ± 2	1.5 ± 0.2
15.15	4.14 ± 0.06	586 ± 6	1.5 ± 0.2
15.20	4.02 ± 0.06	564 ± 6	1.5 ± 0.2
15.25	4.29 ± 0.07	787 ± 8	1.5 ± 0.2
15.30	4.34 ± 0.07	695 ± 7	1.5 ± 0.2
15.70	6.8 ± 0.1	1940 ± 20	-
16.70	-	-	2.7 ± 0.2

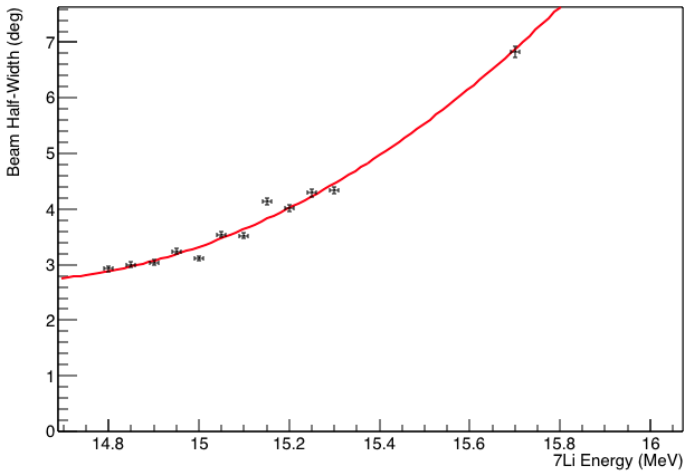

Figure 7.4: Neutron beam half-width as a function of the ^{7}Li bombarding energy.

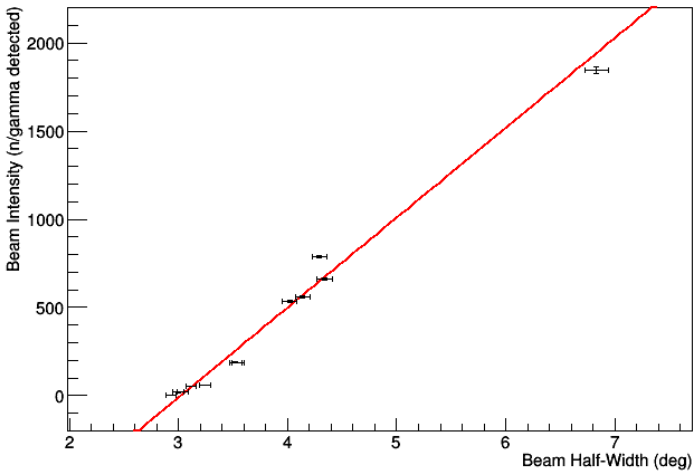

Figure 7.5: Neutron beam intensity versus its half-width.

caused by the energy loss and straggling of ^{7}Li in the target, the two peaks could only be distinguished at 16.70 MeV lithium energy (see Figure 7.6). In this last case thus, the neutron energy was estimated fitting the primary (forward emission) peak, whereas for lower ^{7}Li energies, since the two peaks were overlapped, the overall peak was fitted. The 15.70 MeV run was excluded because the two peaks were separated by little, but it was still impossible to correctly fit just the primary one. Figure 7.6 shows all the three different cases.

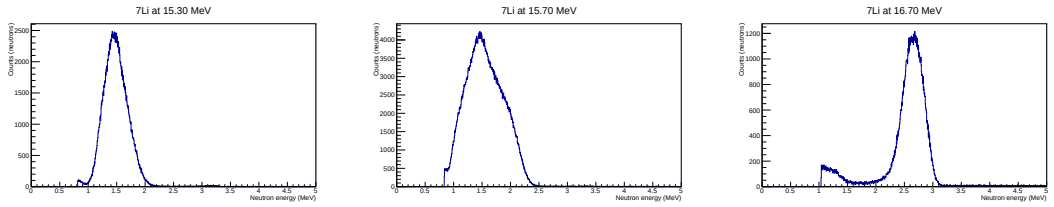

(a) (b) (c)

Figure 7.6: Examples of neutron energy at 0°, changing with lithium energy: (a) 15.30 MeV, (b) 15.70 MeV, (c) 16.70 MeV. The main peak (corresponding to forward emission in the CM) is shifting to the right, to higher energies, while the other one (corresponding to backward emission in the CM) to the left, to lower energies, thus the separation starts to appear. The energy range is cut off at around 1 MeV, since the TOF exceeds the 400 ns time window.

The results are listed in Table 7.1 and displayed in Figure 7.7, alongside with a parabolic fit, which results in:

$$E_n = 0.427(2) \cdot {E_{^7Li}}^2 - 12.81(4) \cdot E_{^7Li} + 97.7(5) \tag{7.3}$$

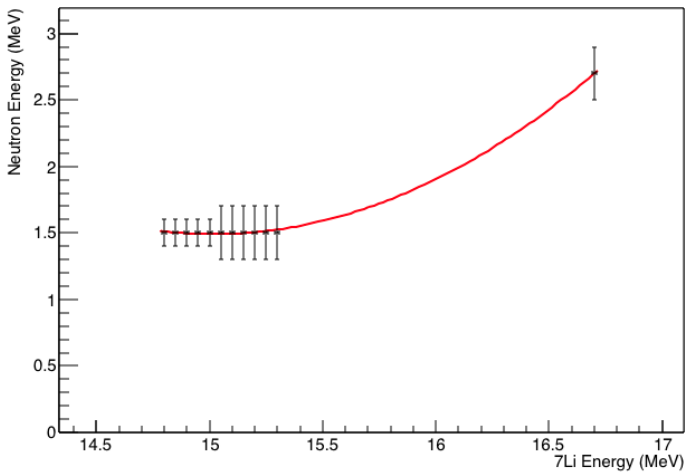

Figure 7.7: Neutron energy at 0° as a function of ^{7}Li bombarding energy.

As said, the energy was calculated from the measured time-of-flight of neutrons, although one aspect needs to be taken into account: the 20 cm length of each NEDA detector doesn't allow an optimal TOF resolution, since it is not possible to know exactly in which part of the detector itself the interaction took place. The distance between the detectors and the source (480 cm) helps to compensate the uncertainty on the actual path, and a first approximation was done considering the centre of the detector as the interaction point.

Finally, the neutron energy angular distribution was analyzed, looking at how the neutron energy changes moving from the centre of the beam towards the edge. The 16.70 MeV run was used in order to be able to distinguish the primary energy peak, and the fit results for each NEDA detector are reported in Table 7.2. They are graphically displayed in Figure 7.8, and a parabolic fit results in:

$$\mathrm{E_n} = -0.004(4) \cdot \phi^2 + 0.01(5) \cdot \phi + 2.7(2) \tag{7.4}$$

where ϕ is the detector angular position.

Table 7.2: Fit results for the neutron energy angular distribution. ^{7}Li at 16.70 MeV.

NEDA detector nr.	**Angular position (deg)**	**Neutron energy (MeV)**
10 (central)	0	2.7 ± 0.2
11	1.58 ± 0.01	2.7 ± 0.2
12	3.15 ± 0.02	2.6 ± 0.2
13	4.73 ± 0.04	2.6 ± 0.2
14	6.30 ± 0.05	2.5 ± 0.2
15	7.88 ± 0.06	2.5 ± 0.2
16	9.45 ± 0.07	2.4 ± 0.2
17	11.03 ± 0.09	2.3 ± 0.2
18	12.6 ± 0.1	2.1 ± 0.2
19	14.2 ± 0.1	1.9 ± 0.2

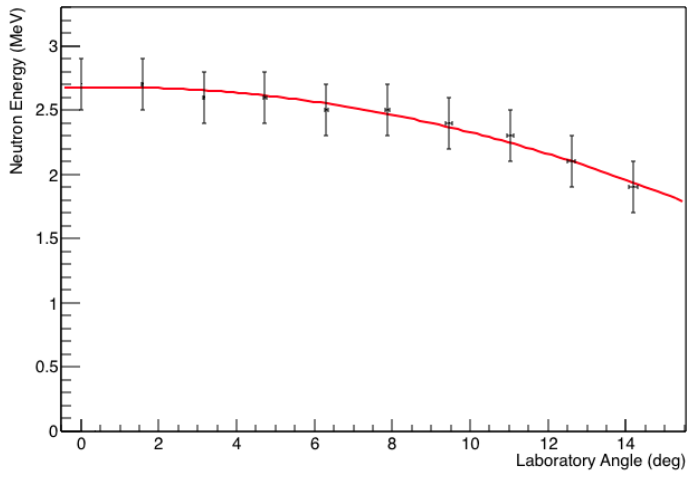

Figure 7.8: Neutron energy angular distribution. ^{7}Li at 16.70 MeV.

8 Neutron image reconstruction

To reconstruct a tomographic image, first of all the sinogram is created, as explained in Section 4. The first object to be analyzed was a compote, due to its simple shape and its low Z elements composition, which assures a strong neutron absorption. The scan lasted 6 h (1 min for each full table translation), with a ^{7}Li energy of 16.30 MeV. The obtained sinogram is shown in Figure 8.1. The shadow of the compote passing back and

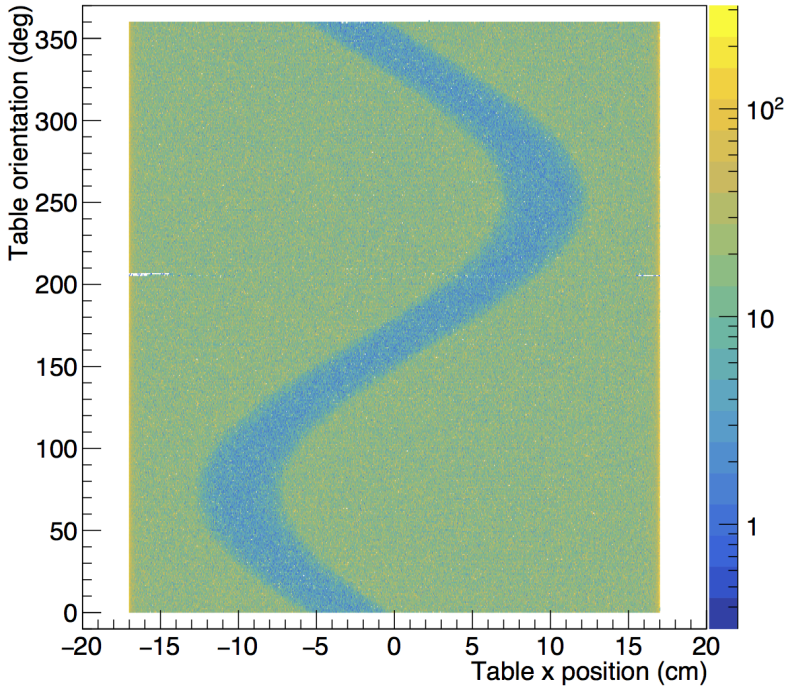

Figure 8.1: Sinogram for a 6 h long scan of a compote, with bombarding ^{7}Li at 16.30 MeV.

forth in front of the neutron beam can clearly be seen.

To pass from the sinogram to a real 2D-image, the algorithm explained in Section 4 was developed, based on the back-projection technique and in particular on the code initially written by Basia Wasilewska. Given the table position x' and orientation ϕ for each registered event by NEDA, the position of the detectors covering angle cone with respect to the table was reconstructed and filled. In the end, after all the different views, the image shown in Figure 8.2 is obtained. A circular shadow corresponding to the shape of the compote is evident, even if there are many halos around it and the image is not well defined yet.

Passing to analyze one of the two unknown metallic boxes, named "Object1", still a 6 h scan was performed, with a lithium energy of 15.25 MeV, and the obtained sinogram

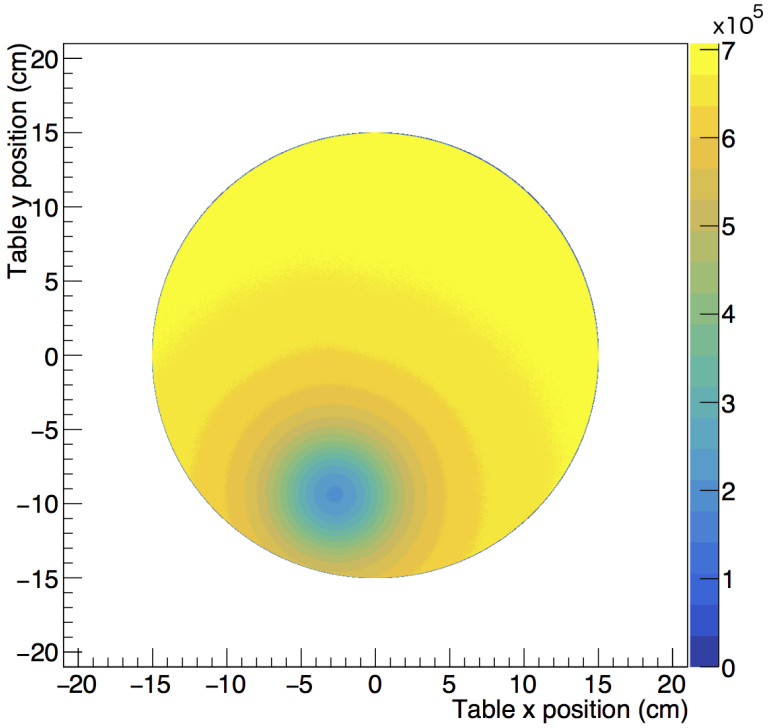

Figure 8.2: Tomographic image reconstruction of the compote, using all the NEDA detectors arc.

is shown in Figure 8.3. It results to be more complicated than the one for the compote,

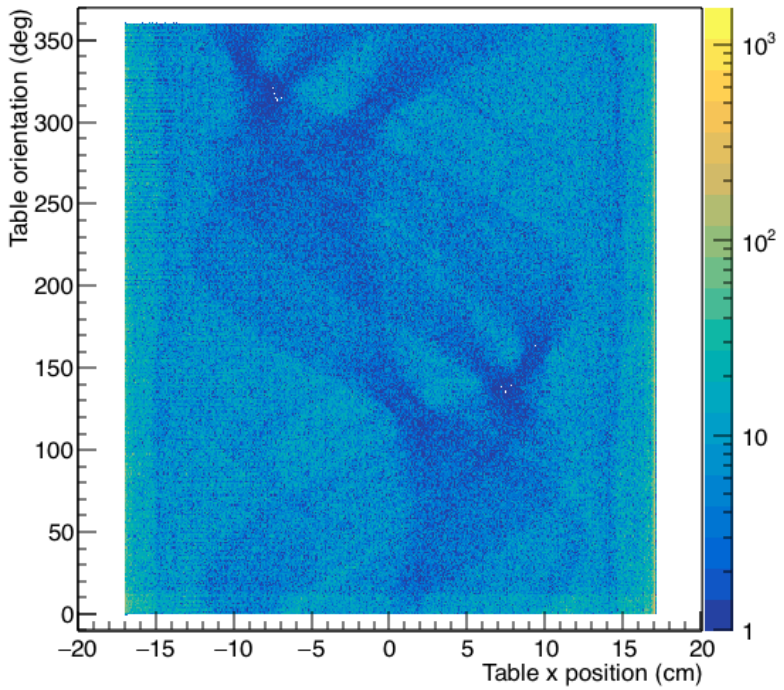

Figure 8.3: Sinogram for a 6 h long scan of the first metallic box with unknown content, with bombarding ^{7}Li at 15.25 MeV.

indicating the presence of several objects inside the metallic box, with probably different and more complicated shapes.

After applying the same algorithm used for the compote, the resulting image can be seen in Figure 8.4. Still, it results to be very blurry, even if the shadows of at least three different objects can be seen.

At this point, several studies were carried out in the analysis phase to try to optimize the image-reconstruction algorithm. First of all, different possible choices of the cone were tried: instead of using all the NEDA detectors, and so their whole covering angle cone, the reconstruction was made with only the detectors involved by the neutron beam. In particular, the NEDA detectors used were the ones being inside the neutron beam width, taken as the FWHM of the corresponding beam profile as discussed in Section 7. The specific cone corresponding to the covering angle of the detector that registered the event was then filled (see Figure 8.5). The obtained image is shown in Figure 8.6, and a slight improvement can be noticed.

Then, only the central NEDA detector was used (and the corresponding cone displayed in Figure 4.5 (c)), resulting in the image of Figure 8.7. As can be seen, even

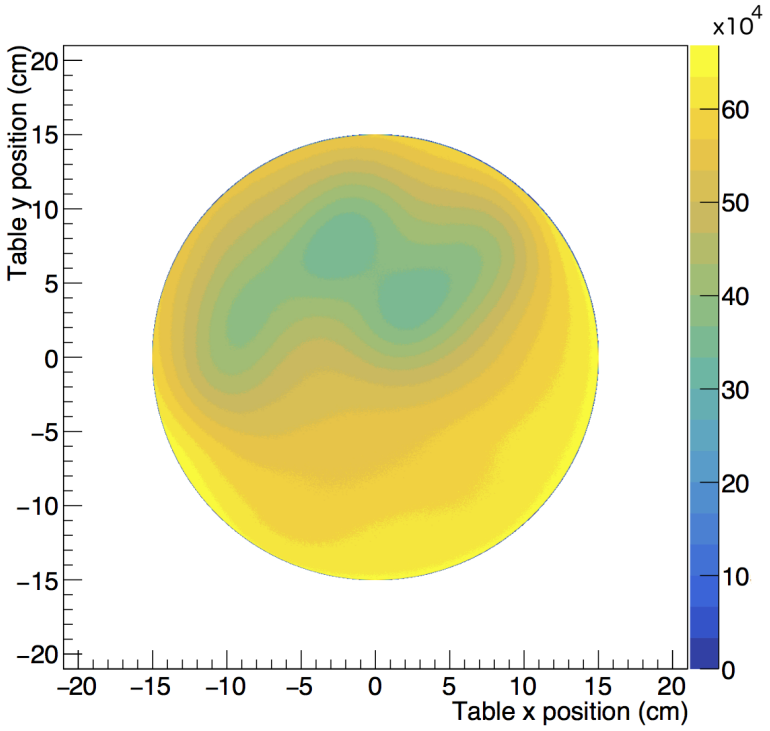

Figure 8.4: Tomographic image reconstruction of the content of the first metallic box, using all the NEDA detectors arc.

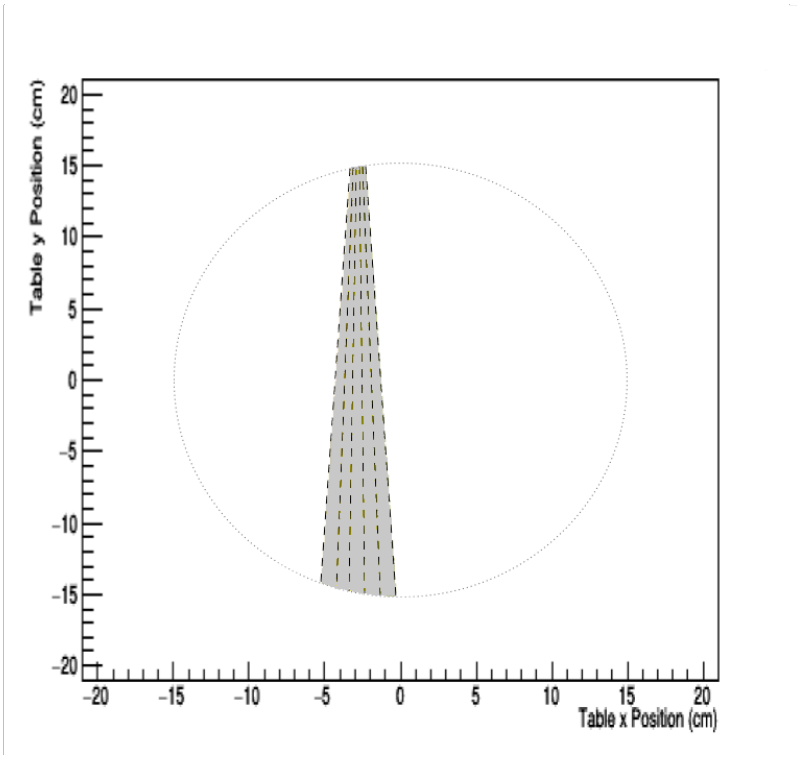

Figure 8.5: Five cones corresponding to the five NEDA detectors inside the neutron beam width. Each one was filled independently, depending on the detector that registered the specific event.

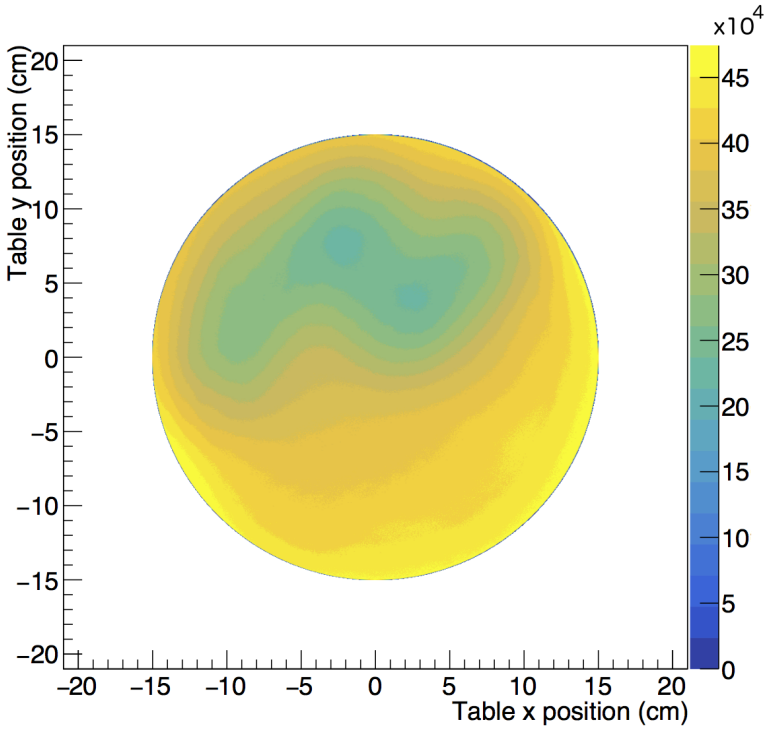

Figure 8.6: Tomographic image reconstruction of the content of the first metallic box, using the NEDA detectors inside the neutron beam cone width.

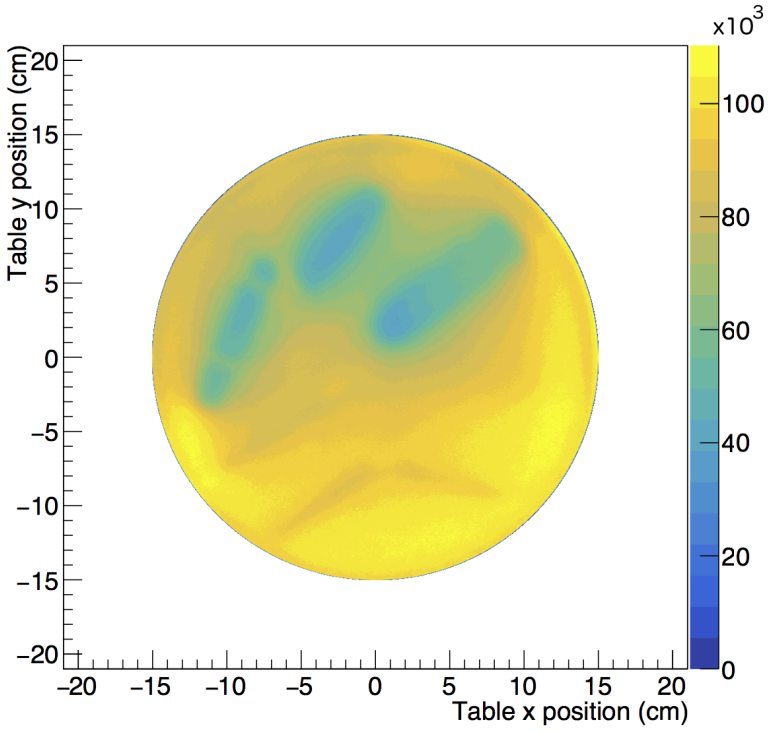

Figure 8.7: Tomographic image reconstruction of the content of the first metallic box, using only the central NEDA detector.

though obviously with less statistics with respect to the whole NEDA array counts ($\sim$ 70% using the detectors inside the beam width, $\sim$ 16% using the central one), the best image resolution by far is achieved using only the central NEDA detector.

Looking at the reconstruction obtained using one of the side detectors (Figure 8.8), i.e. the third to the right of the central one, it is clear why they worsen the overall information on the final image, probably due to the drop in intensity of the neutron beam ($\sim$ 50% for the third from the centre) and the misinformation brought by the scattered neutrons.

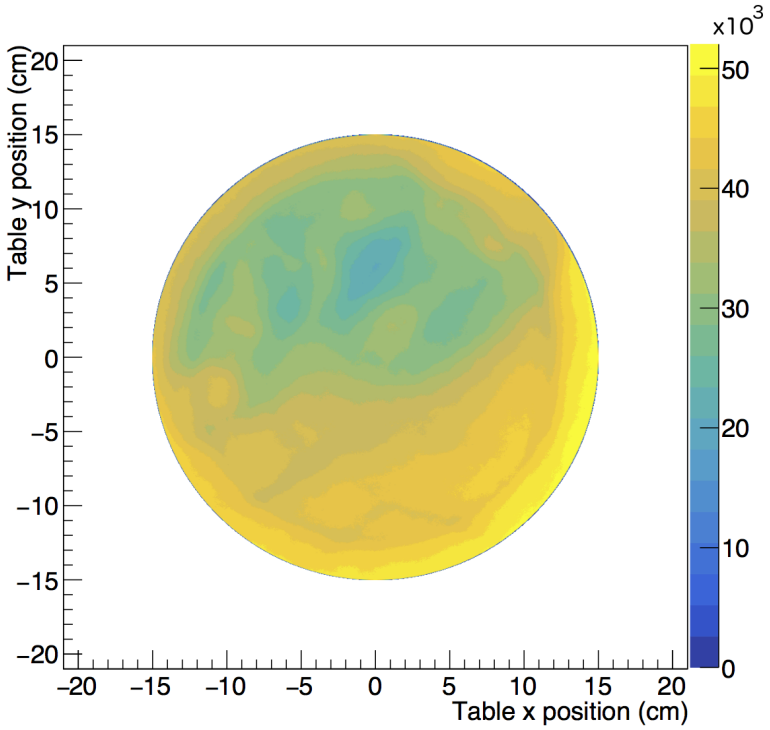

Figure 8.8: Tomographic image reconstruction of the content of the first metallic box, using the twelfth NEDA detector, the one on the edge of the neutron beam width.

Once established that the use of just the central NEDA detector gives the best resolution, two different corrections were studied and implemented in the algorithm to see if they proved to further increase the image resolution.

First, the neutron density along the beam was taken into account: since the diameter of the beam increases moving away from the source, but the number of neutrons in each transversal section must be the same, the neutron density must decrease as the inverse-square of the distance from the source. Considering just the horizontal slice of each circular section, that is what the NEDA arc sees, the density should thus decrease as the inverse of the distance, which is directly proportional to the diameter of the section

itself. For each different y' inside the table, the filling factor was taken as $d_0/d_{y'}$, where d_0 corresponds to the cone diameter at y' = 0, taken as a reference, and $d_{y'}$ to the cone diameter at y'. In Figure 8.9 is shown the reconstruction for one event, using the cone corresponding only to the central NEDA detector.

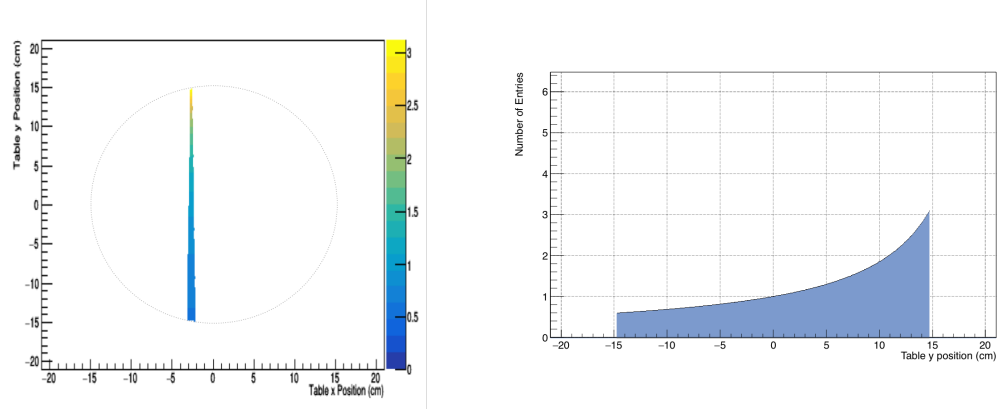

Figure 8.9: One event view reconstruction, using only the central NEDA detector and taking into account the decrease of the neutron density moving away from the source (on the top). On the right it is shown the y-projection of the centre of the cone (the source is on the right).

When applying a correction two important things have to be cared about: first of all, the image resolution should obviously be improved; on the other hand, it is important that the figure is not distorted or falsified. Confronting the reconstructed image before and after the neutron density correction (see Figure 8.10), both the requests are satisfied.

The next correction to be discussed regards the detection efficiency profile of the NEDA detector. In fact, this is not actually uniform along all the cell width, but at a first order it can be assumed linearly decreasing moving from the centre toward the edges, following the behavior of the thickness of the liquid scintillator volume (see Figure 8.11). Thus, for every different y' the resulting weighting function to fill the cone is:

$$f_\epsilon(\text{x'}) = \begin{cases} 0 & \text{if x'} = a \vee \text{x'} = b \ , \\ \frac{1}{2} + \frac{\text{x'}-a}{b-a} & \text{if } a < \text{x'} < \frac{b+a}{2} \ , \\ \frac{1}{2} - \frac{\text{x'}-b}{b-a} & \text{if } \frac{b+a}{2} < \text{x'} < b \ , \end{cases} \tag{8.1}$$

with a and b the x' coordinates of the two cone edges. The comparison with the original image without the correction is shown in Figure 8.12. Again, the image does not result to be distorted and the resolution seems slightly better, even if not major changing can be appreciated.

Finally, the reconstruction algorithm including these two corrections has been applied for all the scanned samples, and the final results are displayed in Figure 8.13. Table 8.1

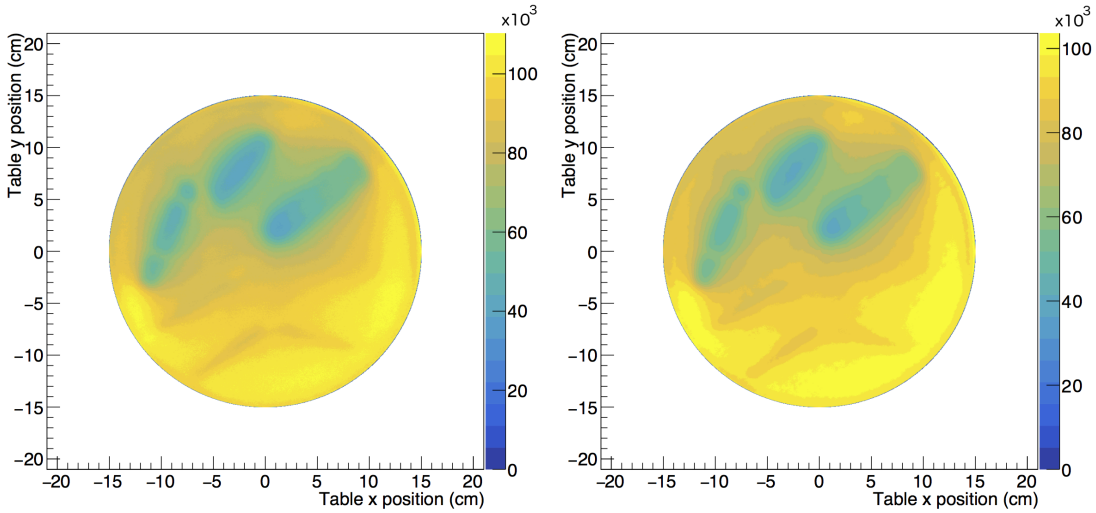

Figure 8.10: Comparison between the tomographic image reconstruction of Object1 before (left) and after (right) the algorithm correction regarding the neutron density along the beam.

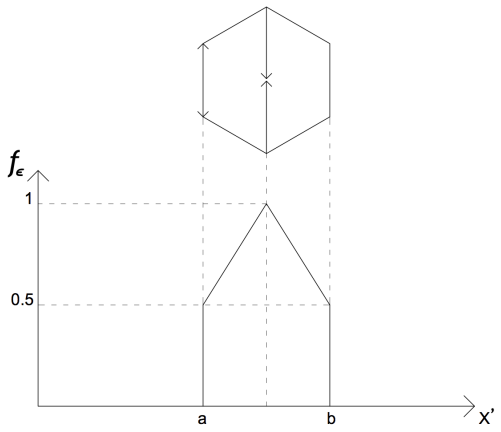

Figure 8.11: NEDA detector efficiency profile as a function of x', estimated considering the volume of liquid scintillator in each vertical slice of infinitesimal width. At the edges of the cell the height of the slice is half the one at the center, due to the hexagonal geometry, and so is the volume.

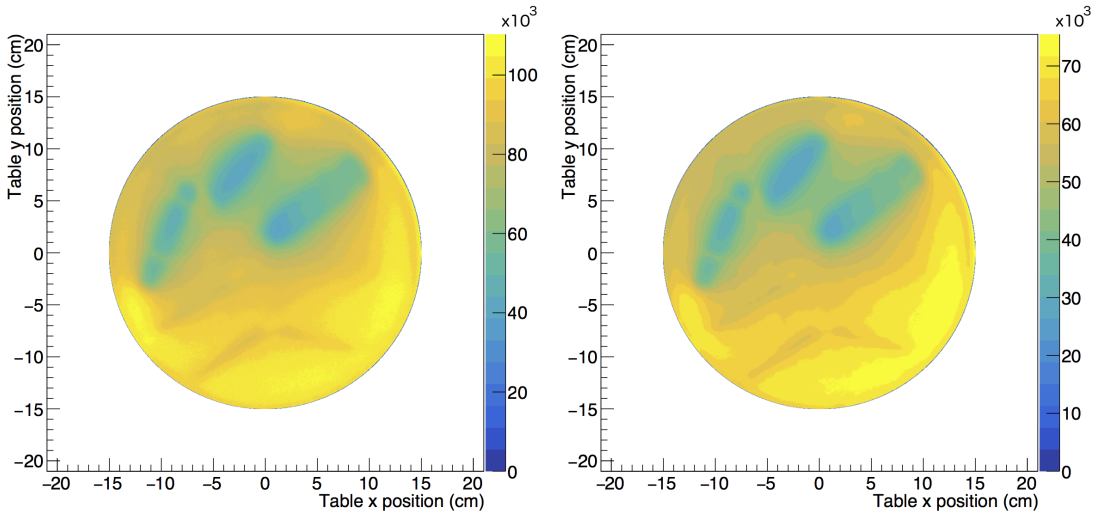

Figure 8.12: Comparison between the tomographic image reconstruction of Object1 before (left) and after (right) the algorithm correction regarding the detection efficiency profile of the NEDA detector.

summarizes the informations for every scan. Notice that for the two heavy metals at the end only a 2 h scan was taken.

Table 8.1: Summary of the scans carried out at IPN Orsay on December 2016.

Sample	**Scan duration**	**^{7}Li energy (MeV)**	**Nr. of events in central NEDA**
Compote	6 h	16.30	1.5×10^{7}
Object1	6 h	15.25	9.4×10^{6}
Object2	6 h	15.25	7.9×10^{6}
Two heavy metals	2 h	15.80	2.1×10^{6}

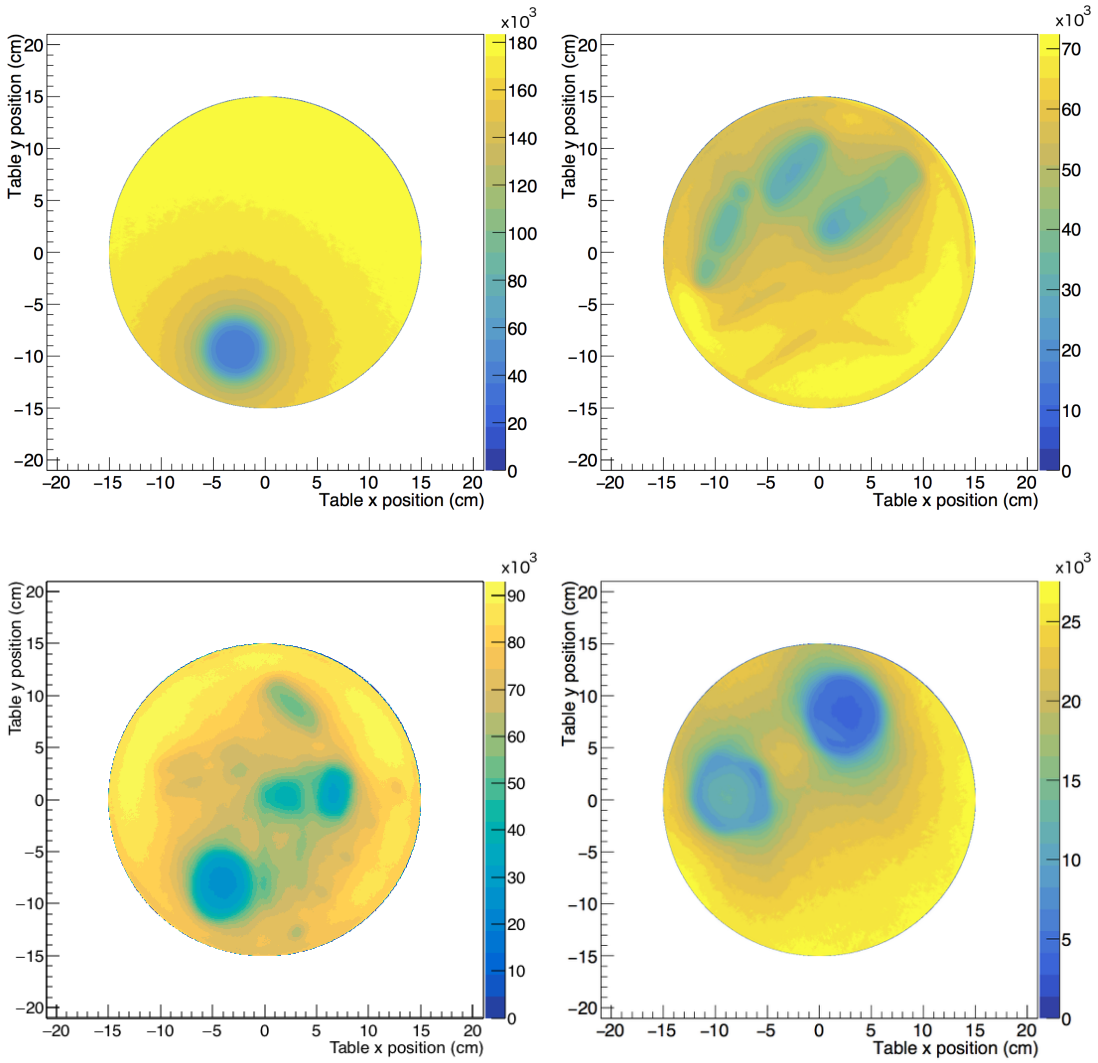

Figure 8.13: Final image reconstruction for the compote (top-left), Object1 (top-right), Object2 (bottom-left), and the two heavy metals (bottom-right), using the central NEDA detector and both the corrections discussed.

9 Gamma image reconstruction

In this work, a totally new technique was developed and tested: the idea consists in exploiting the inelastic scattering that could happen between the produced neutrons and the nuclei of the scanned sample, with the consequent gamma-ray emission (see Figure 9.1).

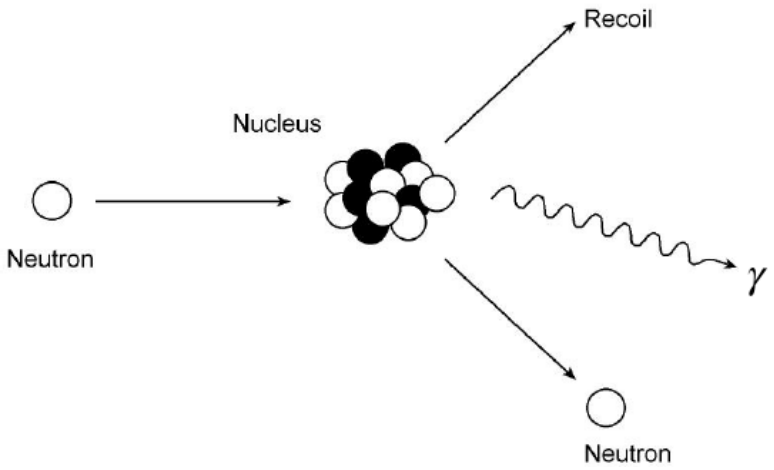

Figure 9.1: Inelastic scattering between a neutron and the nucleus of an atom. In the process a gamma-ray is emitted with an energy characteristic of the particular isotope.

Detecting and identifying the energy of the emitted photon together with the table position and orientation, it should be possible to apply a tomographic reconstruction similar to the one used with neutrons: whenever an event is registered by the Ge detector, the position of the beam cone with respect to the turntable is reconstructed and the event is smeared along the cone itself, as shown in Figure 4.5. In this case, although, the reconstructed image does not indicates the neutron beam absorption, but the gamma emission instead. Also, it is not possible to restrict the analysis to just the central NEDA detector, since the scattering that originated the detected gamma-ray could have taken place everywhere inside the whole neutron beam path. Thus, in the reconstruction algorithm the cone corresponding to the beam width has to be used.

The advantage of this technique consists in the possibility to identify the atomic species present in the sample from the measured gamma-ray energy, and so, combining it with the neutron analysis, obtain a "colored" tomographic image. In fact, if it is possible to identify from which points of the sample the gamma-rays are emitted, the characterization of the different parts in terms of elements composition can be done.

The first excited states of the elements present in the compote (e.g. 4439 keV of ^{12}C and 6049 keV of ^{16}O) are too high in energy to be excited with the ^{7}Li energy used in this experiment (the maximum neutron energy produced is $\sim$ 2.7 MeV, see Table 7.1), while during the two heavy metals run the Ge detector was not operative. Thus, the focus of the analysis was on Object1.

In order to reconstruct the image of the objects using the information given by the Ge detectors, initially a gate on the time-of-flight was performed. In Figure 9.2 (top) it is shown the registered time difference between the Ge detection and the RF for every ^{7}Li beam pulse. In the same figure (bottom), the difference between the energy spectrum on-beam and off-beam can clearly be seen, distinguishing the gamma-rays related with the pulse from the room background. For example, it can be noted the

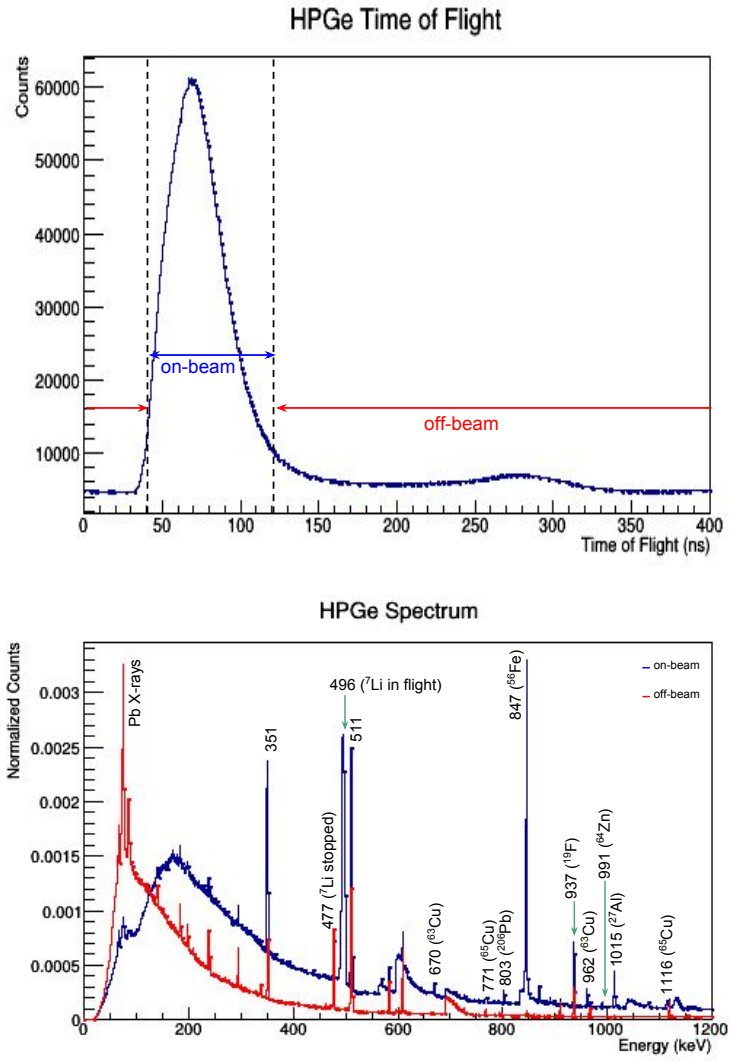

Figure 9.2: Time-of-flight of the events registered by the Ge detector (top), and corresponding on-beam and off-beam energy spectra (bottom) for Object1. The energy spectra are normalized to the integral of the un-gated spectrum.

difference between the two lithium peaks, one at 477 keV and the other at 496 keV, Doppler shifted and broadened. The former is emitted once the stopped ^{7}Be β-decays

into ^{7}Li* (^{7}Be $T_{1/2} \simeq 53$ d), while the latter is emitted in flight after the ^{7}Li(p,p')^{7}Li* reaction (^{7}Li* $T_{1/2} \simeq 73$ fs). It is evident how in the on-beam spectrum (blue) both are present, whereas in the off-beam spectrum (red) the second peak is completely absent. Other peaks are present only in coincidence with the beam pulse (e.g. ^{63}Cu at 670 and 962 keV, ^{56}Fe at 847 keV, ^{27}Al at 1015 keV, etc.), so they must come from the objects hit by the beam.

After making also an energy gate for each one of these peaks, the reconstruction algorithm was applied in order to see if some of them were coming precisely from some spots inside the table. In particular, the energy gate was done for each different element, summing up different peaks belonging to different isotopes. In fact, the major problem of this technique results to be the poor statistics compared to the neutron analysis (4.8×10^4 events for Fe, the strongest line, versus 1.6×10^{10} neutron events using all the NEDA detectors inside the beam width), due to the inelastic scattering probability and the narrow covering angle of the Ge detector.

Once selected the iron line at 847 keV line (with a gate of ±2 keV), in a TOF window between 40 and 120 ns, the sinogram shown in Figure 9.3 was obtained. The minor

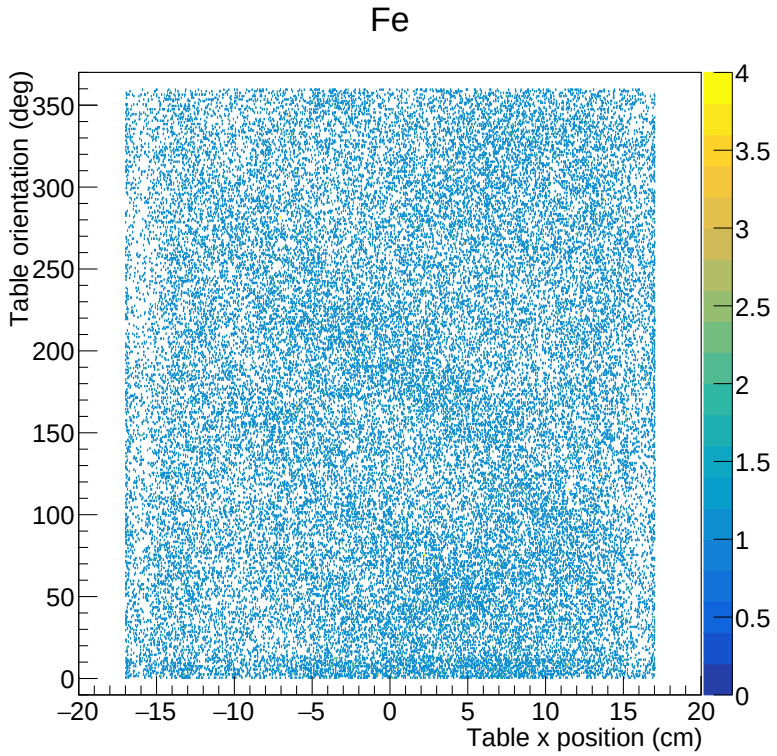

Figure 9.3: Sinogram for Fe detected in a 6 h long scan of Object1, with bombarding ^{7}Li at 15.25 MeV.

statistics results evident, and some small shadows can only hardly be seen. Nonetheless,

when applying the algorithm to reconstruct the two-dimensional image, a spatial correlation between the origin of the Fe gamma-rays and some regions inside the object is evident (see Figure 9.4).

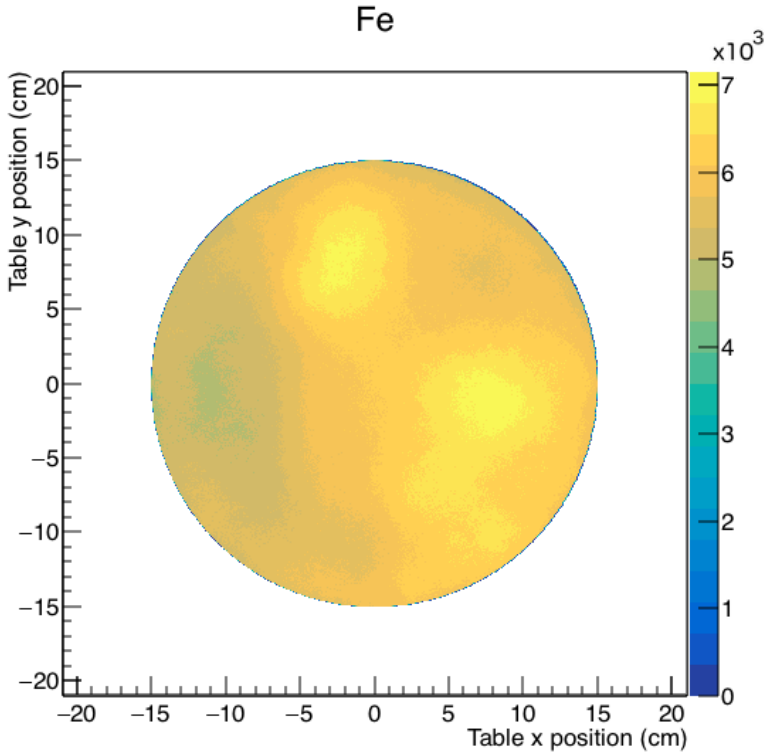

Figure 9.4: Tomographic image reconstruction for Fe in Object1, without any correction.

Now, as done for the neutron image reconstruction, several corrections were studied. In particular:

1. Neutron density along the beam.
2. Beam profile.
3. Background subtraction.
4. Detection probability with respect to the distance from the Ge detectors.
5. Neutron absorption profile from neutron image reconstruction.
6. Neutron scattering probability from neutron image reconstruction.

1. The first correction, regarding the conservation of the number of neutrons, was applied in the same way as in the neutron reconstruction (see Figure 8.9), with the exception of using all the NEDA detectors inside the beam width instead of only the

central one. The comparison between the reconstruction before and after the correction is shown in Figure 9.5. Significant improvement can not be seen, just a small better definition of the blob on the right in particular. Anyway, the image does not result distorted, so the correction seems acceptable.

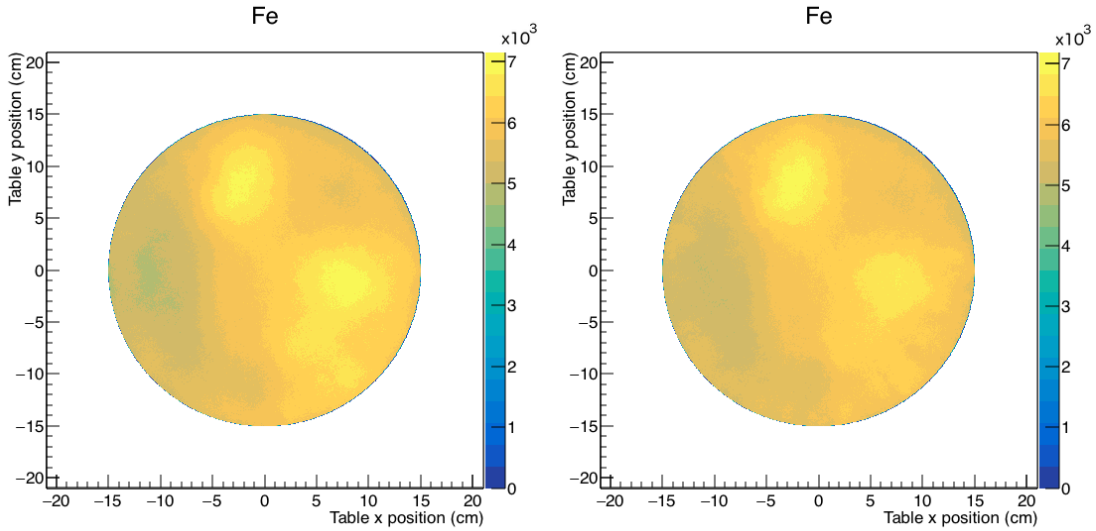

Figure 9.5: Comparison between the tomographic image reconstruction of Fe in Object1 before (left) and after (right) the algorithm correction regarding the neutron density along the beam.

2. After that, the neutron beam profile was taken into account. As shown in Figure 9.6, the cone was divided in smaller ones, corresponding to the covering angle of the different NEDA detectors; each one was filled with a factor equal to the respective measured neutron intensity, normalized to the center: $f_2 = I_i/I_c$. In Figure 9.7 the reconstruction after the correction can be seen in comparison with the original image. Also in this case, a slight improvement can be seen.

3. For the background subtraction, an image was reconstructed gating on the gamma-background just before and after the selected energy peak (see Figure 9.8), making an average between the two. Then, the resulting image was subtracted to the one obtained gating on the peak. After the subtraction, the image changes as shown in Figure 9.9, and the same observations as for the previous corrections can be made.

4. Taking into account the different distance of each point inside the cone from the Ge detector, and so the different ratio between the detection area and the corresponding whole 4π spherical surface, the probability that the emitted gamma ends up into the germanium is inversely proportional to the square of the distance. In fact, considering the former as constant, the latter depends on the square of the radius of the sphere, i.e. the distance from the point and the detector; taking now the above-mentioned probability as the ratio between the two areas, the result follows. Referring to Figure 9.10, treating the problem in a 2D-approximation, in other words excluding the x' component which

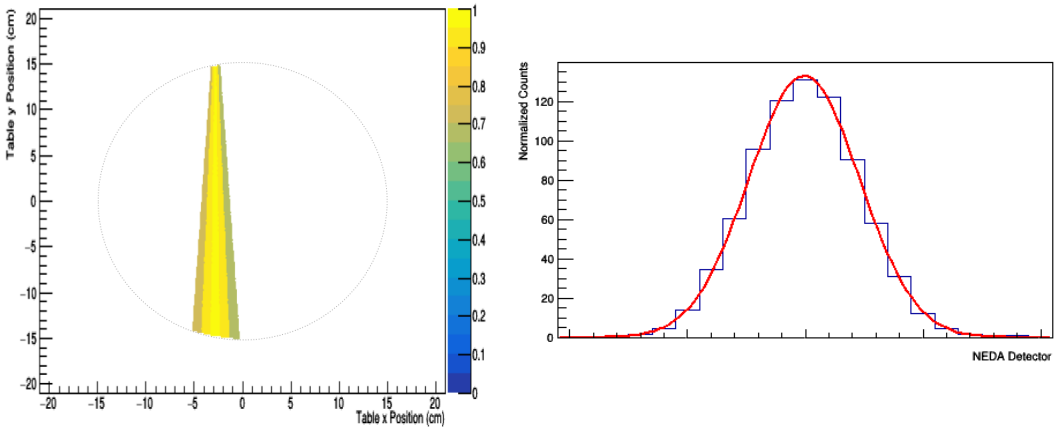

Figure 9.6: One event view reconstruction considering the neutron beam profile, which is shown on the right as it has been measured by the NEDA detectors for the given ^{7}Li energy of 15.25 MeV. As before, only the cone width corresponding to the FWHM was taken into account.

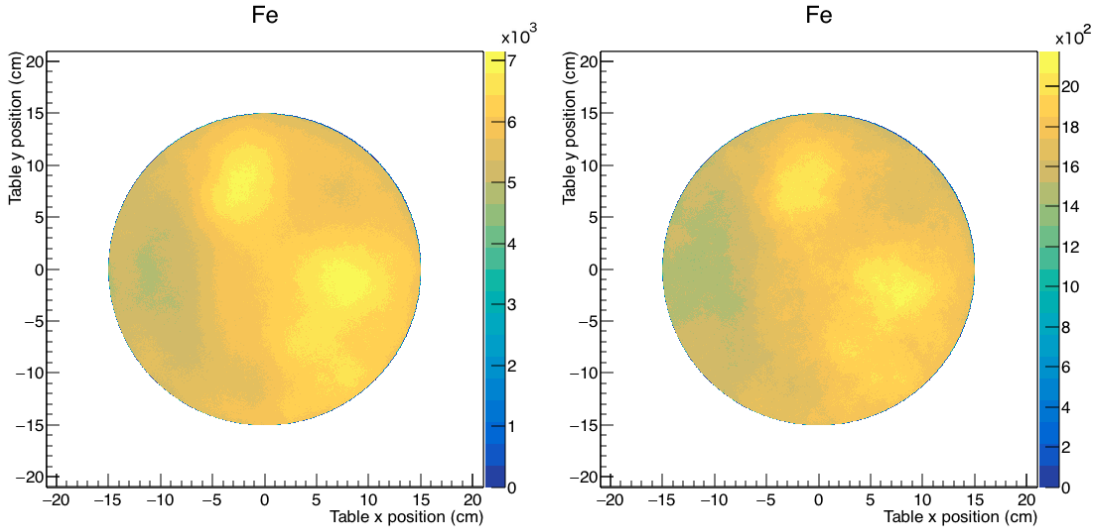

Figure 9.7: Comparison between the tomographic image reconstruction of Fe in Object1 before (left) and after (right) the algorithm correction regarding the neutron beam profile.

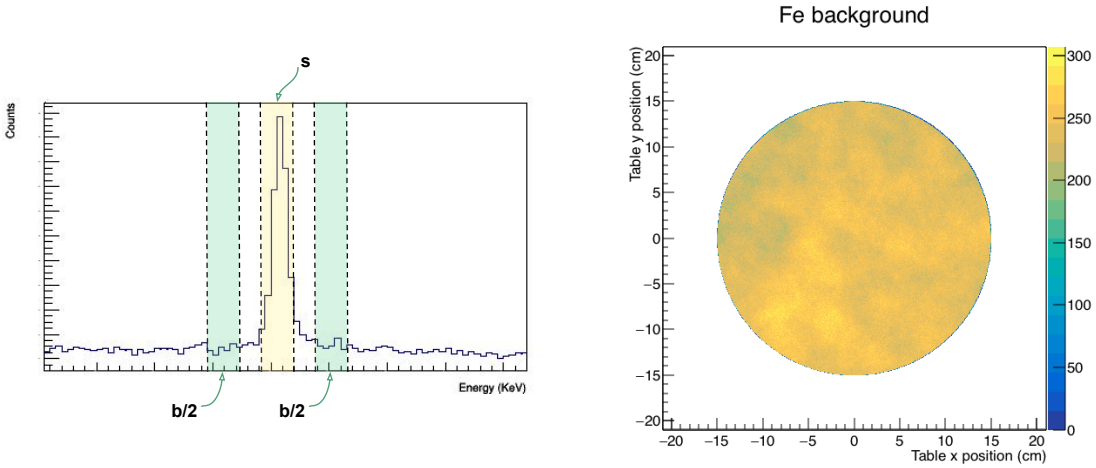

Figure 9.8: On the left the different gates used for the background subtraction are shown: the one in yellow is the energy gate on the selected peak, while the two in green correspond to the gates on the background. On the right the image corresponding to the Fe background is presented.

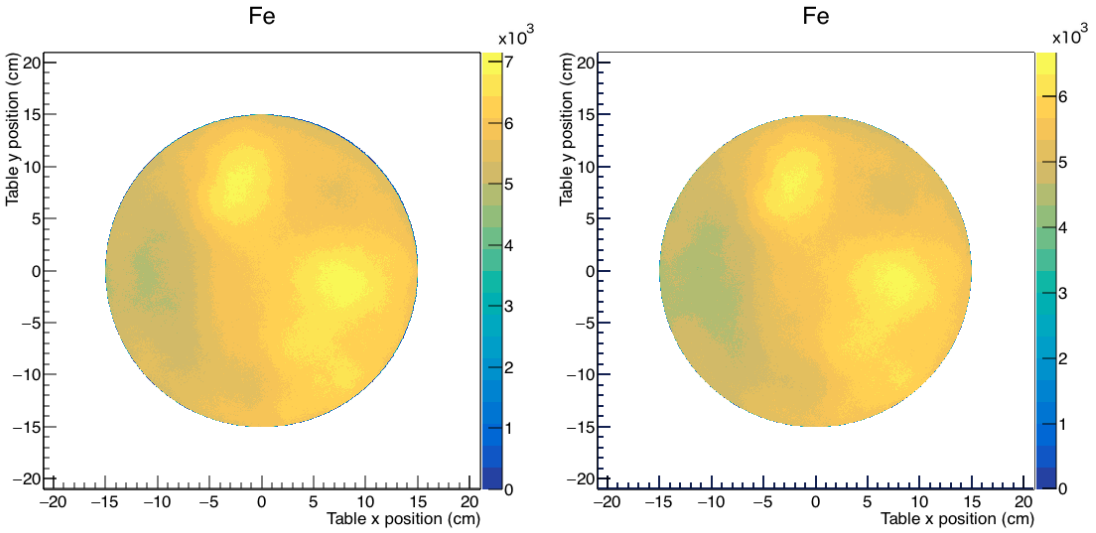

Figure 9.9: Comparison between the tomographic image reconstruction of Fe in Object1 before (left) and after (right) the background subtraction.

is small, it results $d^2 = h^2 + y'^2$, and each point inside the cone was filled with a factor $f_4 = h^2/d^2$. As can be seen in the comparison in Figure 9.11 although, the image after

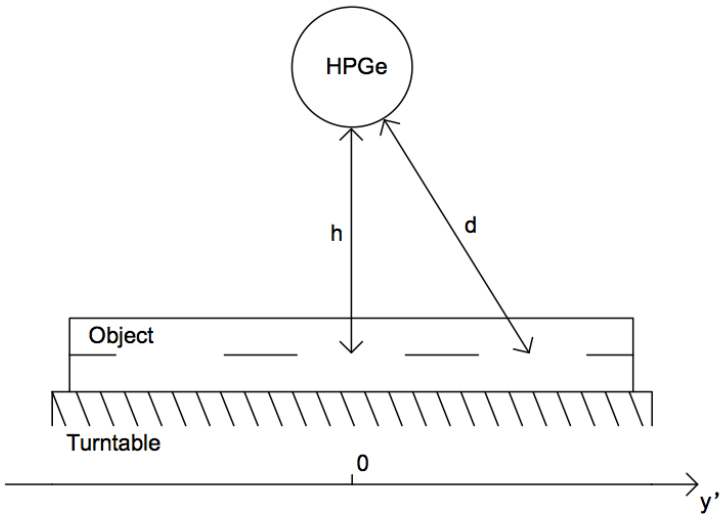

Figure 9.10: Scheme of a side view of the scanned object, the turntable and the Ge detector.

the correction results distorted, amplifying too strongly the central region compared to the outer one. Thus, this correction was discarded.

5. The idea now is to exploit the information obtained by the neutron absorption: for each (x, y) inside the cone, a filling factor was calculated corresponding to the probability that a neutron had reached that point without being absorbed by the object. For every point, the reconstructed neutron image was rotated in the same table position; then, a factor $f_5 = S_{(x,\,y)}/S_{max}$ was calculated, where $S_{(x,\,y)}$ corresponds to the sum of the content of each point along the path that connects the source to (x, y) (see Figure 9.12), and S_{max} to the integral along the same path of the value corresponding to no absorption, taken as the maximum bin content. In practice, $S_{(x,\,y)}/S_{max}$ represents the percentage of neutron transmission through the object until the point (x, y). Also in this case, as can be seen in Figure 9.13, the correction seems to distort the image and it was not taken into account.

6. Finally, using again the reconstructed neutron image, the neutron scattering probability was considered. In each point inside the cone, the percentage of neutron absorption was obtained considering the factor $f_6 = 1 - c_{(x,\,y)}/c_{max}$, where $c_{(x,\,y)}$ and c_{max} are the content of the corresponding (x, y) point and the maximum bin content in the neutron image respectively. This factor was considered as the scattering probability between a neutron and a nucleus of the sample, hence the probability that the gamma-ray originated from (x, y). However, the correction seems to affect too strongly the reconstruction (see Figure 9.14), in other words the information from the neutron

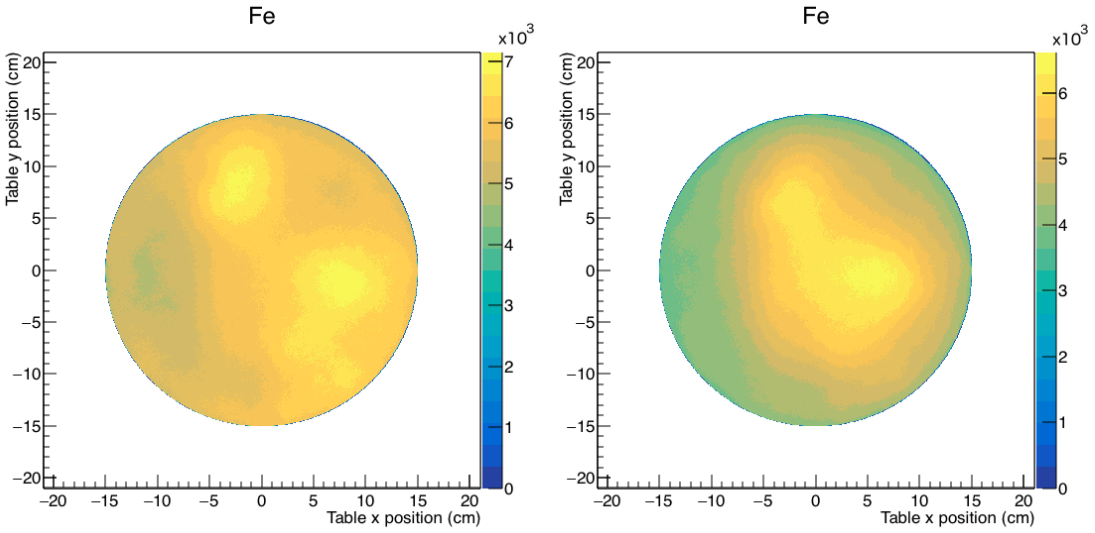

Figure 9.11: Comparison between the tomographic image reconstruction of Fe in Object1 before (left) and after (right) the algorithm correction regarding the distance from the Ge detector.

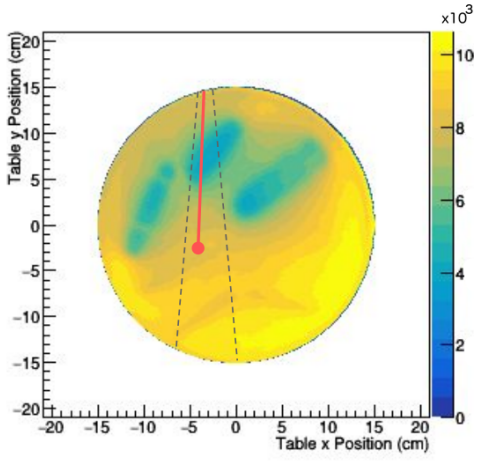

Figure 9.12: Representation of the path from the source to a point (x, y) in the neutron image.

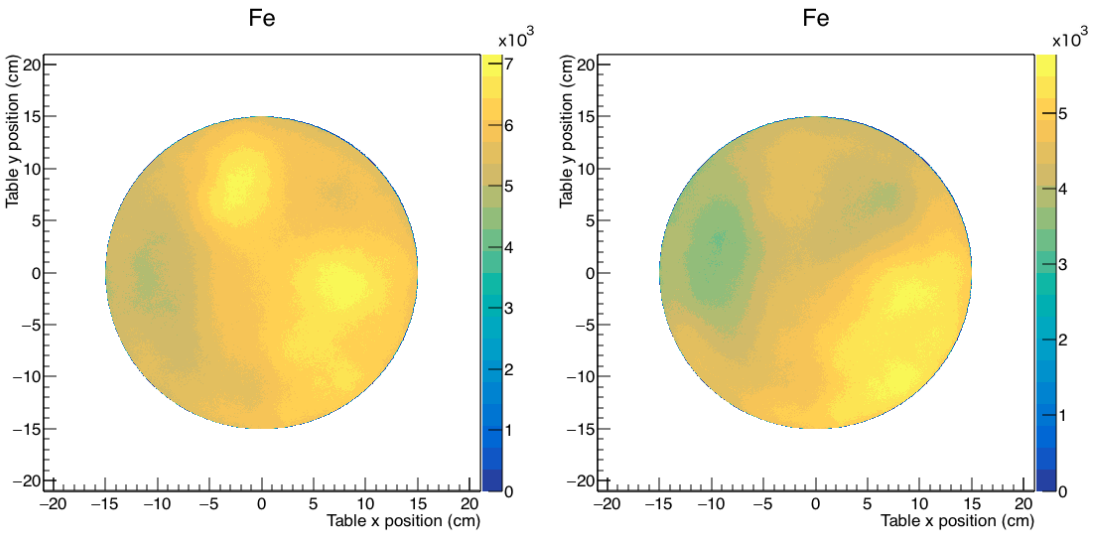

Figure 9.13: Comparison between the tomographic image reconstruction of Fe in Object1 before (left) and after (right) the neutron absorption information obtained from the neutron reconstruction.

reconstruction overrides the information from the gamma detection, probably due to the much greater statistics and better resolution. Thus, even this last correction was discarded in the analysis.

To summarize the corrections studied for the gamma image reconstruction and the result of their goodness:

1. Neutron density along the beam. ✓
2. Beam profile. ✓
3. Background subtraction. ✓
4. Detection probability with respect to the distance from the Ge detectors. ×
5. Neutron absorption profile from neutron image reconstruction. ×
6. Neutron scattering probability from neutron image reconstruction. ×

Adding the selected corrections to the final algorithm, different images were reconstructed for different elements (see Table 9.1), and the results are shown in Figure 9.15. The last two elements, ^{27}Al and ^{206}Pb, are present in the table itself and the LICORNE beam stopper respectively, thus the corresponding image should be almost uniform throughout the table, as it is. Notice that Cu and Zn are coming from the same spot of the table, indicating that probably there is a brass alloy in that position.

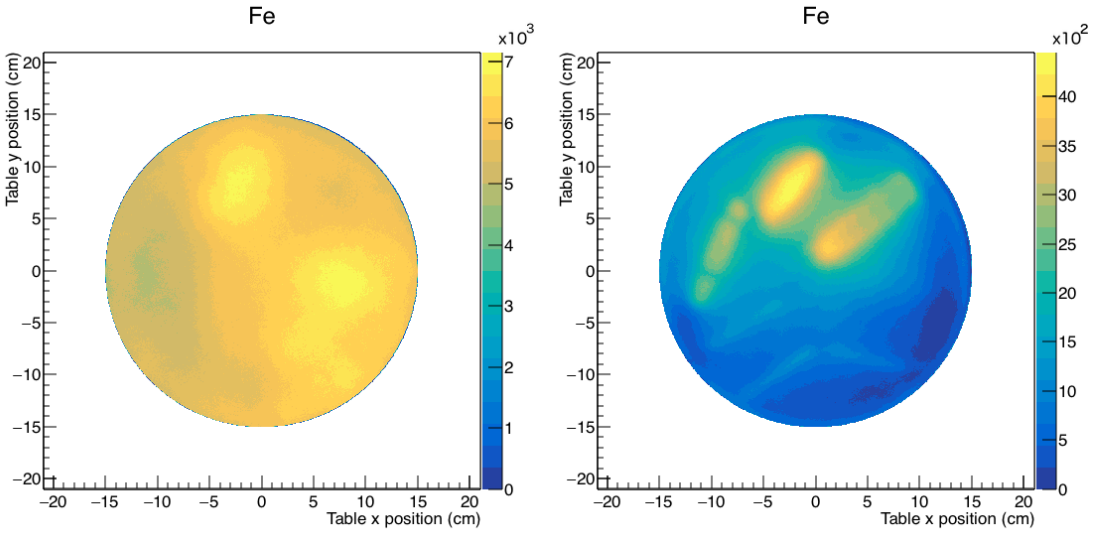

Figure 9.14: Comparison between the tomographic image reconstruction of Fe in Object1 before (left) and after (right) the algorithm correction regarding the neutron scattering probability obtained from the neutron reconstruction.

Table 9.1: Summary of the analyzed elements present in Object1.

Element	**Z**	**Isotope**	**Abundance**	**First excited states (keV)**	**Nr. of events**
Fe	26	^{56}Fe	92%	847	4.8×10^4
Cu	29	^{63}Cu	69%	670, 962, 1327	1.8×10^4
		^{65}Cu	31%	771, 1116	
Zn	30	^{64}Zn	49%	991	6.8×10^3
Al	13	^{27}Al	100%	1015	1.3×10^4
Pb	82	^{206}Pb	24%	803	4.3×10^3

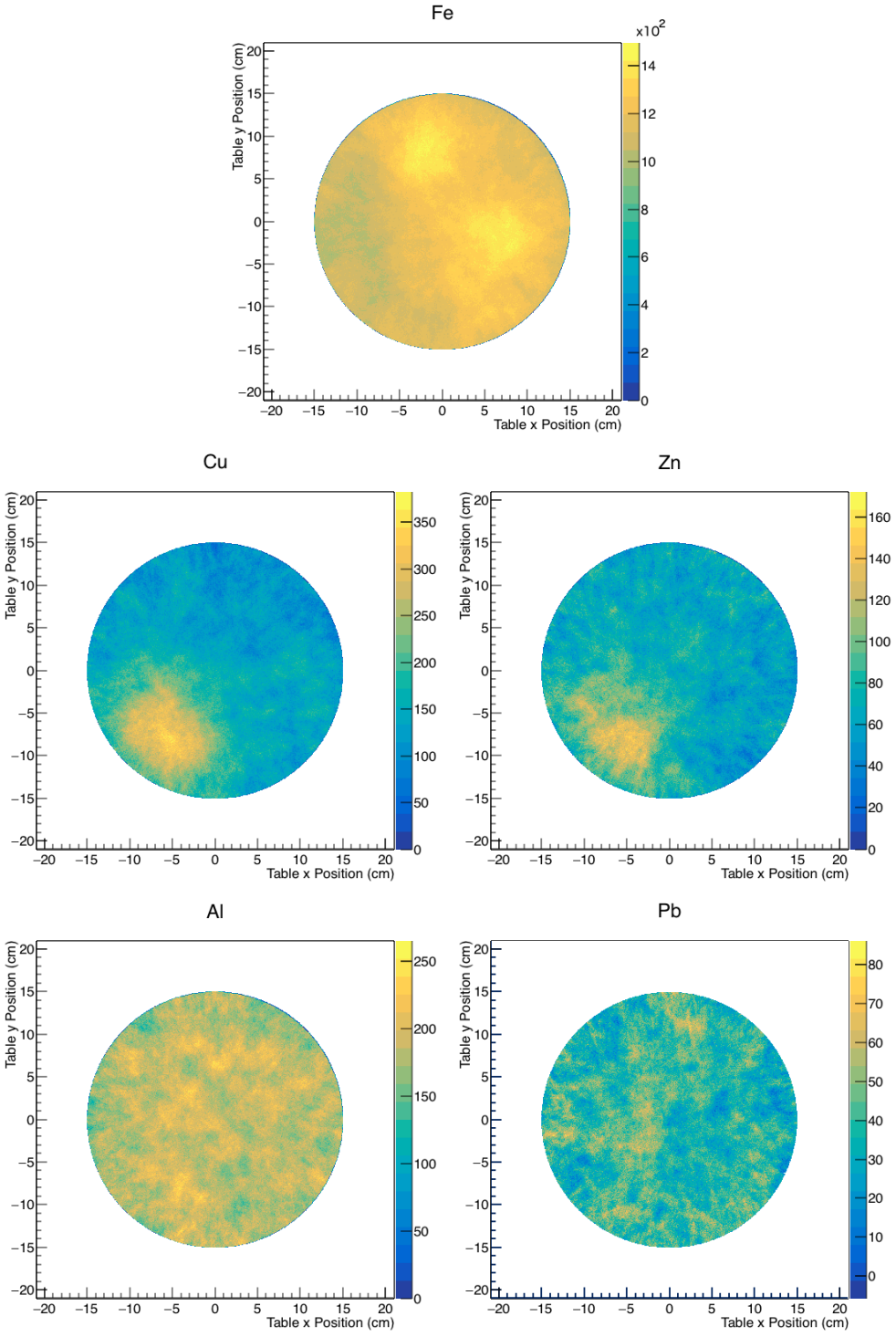

Figure 9.15: Final gamma image reconstruction for Fe (top), Cu (top-left), Zn (top-right), Al (bottom-left), Pb (bottom-right) detected in Object1.

10 Summary and Conclusions

In this work, the feasibility to perform a tomographic imaging with the fast neutron beam produced by the unique directional neutron source LICORNE was studied. In particular, the neutron beam was produced exploiting the inverse kinematic reaction p(^{7}Li,n)^{7}Be, which allows for both a good degree of collimation ($< 5°$) and a high neutron flux (up to 10^7 neutrons/s/sr). For the neutron detection, the new generation NEutron Detector Array NEDA was used. This permitted also to measure in real-time the produced neutron beam in its whole width, hence a study of the beam itself was performed too, in terms of geometry, neutron energy production and neutron energy angular distribution. Beam with an half-width of less than 3° could easily be produced with the lowest ^{7}Li energies (near the reaction threshold), and the corresponding neutron energy at 0° was of about 1.5 MeV. With a ^{7}Li of 16.7 MeV, neutron energies up to 2.7 MeV could be reached, even if the degree of collimation of the beam dropped.

Alongside the neutron tomographic reconstruction, a totally new technique was thought and tested: detecting the gamma-rays emitted after the inelastic scattering between the produced neutrons and the nuclei of the scanned sample, it should be possible to identify the elements distribution inside the object, opening the possibility for a new kind of tomography.

The setup saw the LICORNE neutron source operating in a ^{7}Li energy range between 14.80 and 16.70 MeV, with a pulsed beam of about 20 nA. At a distance of 6.75 cm from the LICORNE exit window there was the 15 cm diameter turntable, specifically designed to be able to rotate in angle with 1° steps and shift in the direction perpendicular to the beam axis by up to 15 cm in both directions, with about 3 mm steps. An arc of nineteen NEDA detectors, for a total length of 2.5 m, was placed 4.8 m away from the neutron source, covering a 30° angle in the horizontal plane, about 1.5° for each detector. 13 cm above the turntable, one Ge detector (the second one did not prove to work) detected the gamma-rays coming from the scanned samples. These were respectively a compote, two cylindrical metallic boxes with unknown contents, and two heavy metals with paraffin with simple geometric shapes. The duration of each scan was 6 hours, except for the two heavy metals where only a 2 hours scan was performed. The read-out of the detectors was carried out with Faster 12-bits 500 Msps digitizers.

A specific algorithm for the tomographic image reconstruction was developed, based on the *back-projection* technique, and different corrections were also studied. For the neutron image, the best image resolution was achieved using only the central NEDA detector, probably due to the lower statistics at the edges of the neutron beam and the misinformation from the scattered neutrons. In any case, about 23% of the intensity is contained in the center of the beam. Including both the decreasing neutron density along the beam and the detector detection efficiency profile proved to slightly improve the final result. In the end, good images were obtained for all the scanned objects, and in particular a spatial resolution of ~ 1 cm could be achieved (as can be seen by the five aligned dots at the bottom-right in Object2, or the pentagonal edge of one of the two heavy metals). Both a further resolution improvement and the halos removal in the

reconstructed images can be obtained using a more advanced reconstruction method, as the *filtered back-projection* technique, or the *Simultaneous Iterative Reconstruction Technique* (SIRT) [25, 26].

The same algorithm proved to work also for the gamma tomographic imaging, even though a worse resolution was found due to far lesser statistics and the constraint to use the entire neutron beam width. The statistics could be doubled if both the Ge detectors worked properly, and the ideal situation would be with a ring of Ge detectors all around the turntable. After several corrections were studied for Object1, iron and brass presence was found in different locations, proving the feasibility of this new technique, that could be used in conjunction with the neutron tomography.

Possible further improvements that had already been thought could be a Ge detector lead shielding from the room background, allowing to pass only the gamma-rays from the scanned object, as well as reducing the effective neutron beam width, for example using a thinner tantalum foil (e.g. 2 μm) that causes the ^{7}Li struggling, or through a collimator placed right after the LICORNE exit window. This should dramatically improve the tomographic image resolution also for the gamma analysis, just as it did for the neutron one when passing from using all the beam width to just the central NEDA detector.

The results of this first analysis seem to prove nonetheless the goodness of the tomographic imaging with LICORNE fast neutron beam and the feasibility of elements recognition and localization inside the sample, opening the possibility for a completely new way to examine materials.

References

[1] J. N. Wilson, M. Lebois, P. Halipre, et al. "LICORNE: A new and unique facility for producing intense, kinematically focused neutron beams at the IPN Orsay". In: *EPJ Web of Conferences* (2013), p. 62.

[2] A. Pipidis, A. Di Nitto, G. Jaworski, et al. "The genesis of neda (neutron detector array): characterizing its prototypes". In: *LNL Annual report* (2010), p. 78.

[3] Steven W. Smith. *The Scientist and Engineer's Guide to Digital Signal Processing.* California Technical Publishing, 1997.

[4] M. Lebois, J.N. Wilson, et al. "Development of a kinematically focused neutron source with the p(^{7}Li,n)^{7}Be inverse reaction". In: *Nuclear Instruments and Methods in Physics Research A 735* (2014), p. 145.

[5] M. Drosg. *The $^1H(^7Li,n)^7Be$ Reaction as a Neutron Source in the MeV Range.* Technical Report. Los Alamos National Laboratory, 1981.

[6] J. Dave et al. In: *Nuclear Instruments and Methods in Physics Research A 200* (1982), p. 285.

[7] M. Drosg. *Monoenergetic neutron production by two body reactions in the energy range from 0.0001 to 500 MeV.* Debrecen, Hungary: TCM-Meeting of IAEA, 1999.

[8] J. N. Wilson, M. Lebois, et al. "Prompt emission in fission induced with fast neutrons". In: *Physics Procedia 64* (2015), p. 107.

[9] G. F. Knoll. *Radiation Detection and Measurement - 3rd edition.* John Wiley & Sons, 1999.

[10] R. K. Hobbie and B. J. Roth. *Intermediate Physics for Medicine and Biology.* Springer, 2007.

[11] J. N. Wilson, M. Lebois, et al. "LICORNE: A new and unique facility for producing intense, kinematically focused neutron beams at the IPN Orsay". In: *EPJ Web of Conferences 62* (2013).

[12] G. Jaworski et al. In: *Nuclear Instruments and Methods in Physics Research A 673* (2012), p. 64.

[13] T. Hüyük et al. In: *European Physical Journal A* (2016), p. 52.

[14] S. Akkoyum et al. "AGATA, Advanced gamma tracking array". In: *Nuclear Instruments and Methods in Physics Research A 668* (2012), p. 26.

[15] J. Simpson et al. In: *Acta Physica Hungarica: Heavt Ion Physics 11* (2000), p. 159.

[16] J. J. Valiente Dobón, D. Mengoni, et al. In: *LNL-INFN Annual Report* (2014), p. 95.

[17] *NEUTRON/GAMMA PSD EJ-301, EJ-309.* 2017. URL: `http://www.eljentechnology.com/products/liquid-scintillators/ej-301-ej-309`.

[18] D. Renker. "New developments on photosensors for particle physics". In: *Nuclear Instruments and Methods in Physics Research* (2009).

[19] A. Raggio et al. “Timing Characterization of the NEDA Detector”. In: *LNL-INFN Annual Report* (2016).

[20] A. Raggio et al. “Pulse Shape Analysis of the NEDA Detector”. In: *LNL-INFN Annual Report* (2016).

[21] *Fast Acquisition System for nuclEar Research*. 2017. URL: `http://faster.in2p3.fr/`.

[22] P. A. Soderstrom, J. Nyberg, and R. Wolters. “Digital pulse-shape discrimination of fast neutrons and gamma rays”. In: *Nuclear Instruments and Methods in Physics Research A 594* (2008).

[23] M. Moszynski et al. “Study of n-γ discrimination by digital charge comparison method for a large volume liquid scintillator”. In: *Nuclear Instruments and Methods in Physics Research A 317* (1992).

[24] X. L. Luo, V. Modamio, J. Nyberg, et al. “Test of digital neutron-gamma discrimination with four different photomultiplier tubes for the NEutron Detector Array (NEDA)”. In: *Nuclear Instruments and Methods in Physics Research A 767* (2014).

[25] P. A. Penczek. “Fundamentals of three-dimensional reconstruction from projections”. In: *Methods Enzymol* (2010).

[26] E. F. Oliveira et al. “Comparison among tomographic reconstruction algorithms with limited data”. In: *2011 International Nuclear Atlantic Conference* (2011).